UNIVERSITY OF OKLAHOMA

GRADUATE COLLEGE

DYNAMICS OF A SMALL BODY AROUND ASTEROID (29075) 1950DA

A THESIS

SUBMITTED TO THE GRADUATE FACULTY

in partial fulfillment of the requirements for the

Degree of

MASTER OF SCIENCE

By Evan Andrew Blosser
Norman, Oklahoma
2025

DYNAMICS OF A SMALL BODY AROUND ASTEROID (29075) 1950DA

A THESIS APPROVED FOR THE

SCHOOL OF AEROSPACE AND MECHANICAL ENGINEERING

BY THE COMMITTEE CONSISTING OF

DR. DIOGO MERGUIZO SANCHEZ, CHAIR

DR. PRAKASH VEDULA

DR. WEI SUN

UNIVERSITY OF OKLAHOMA

Abstract

Norman Astrodynamics Research Group
Gallogly College

Master of Science in Aerospace Engineering

Dynamics of a Small Body Around Asteroid (29075) 1950DA

by Evan BLOSSER

This thesis presents a comprehensive study on the dynamics of a small body around the near-Earth asteroid (29075) 1950 DA. The research focuses on developing accurate gravitational models for irregularly shaped small bodies, utilizing the Mass Concentration (MASCON) method and verifying this with previous works on the asteroid (99942) Apophis. The results demonstrate the validity of the MASCON model implemented in this work. The model is then used to analyze the orbital dynamics around 1950 DA, identifying possible resonance and periodic orbits around the asteroid. The study forms a preliminary mission design to the asteroid 1950DA, focusing on equilibrium points, capture orbits, scanning orbits, and potential landing sites. No equilibrium point was found, yet ΔV analysis was performed for the preliminary mission design showing the viability of any future mission to the asteroid. The study also examines the possibilities of utilizing machine learning to reduce the models computational load, while highlighting the significant errors the reduced model has. Finally the study examines the rotation dynamics of the asteroid and its impact on the asteroids composition and possible ring formation around the equatorial plane.

Acknowledgements

I would like to give special thanks to my advisor Dr. Diogo Merguizo Sanchez for his continued support and guidance throughout both my undergraduate and graduate research career. Giving me the opportunity, despite my less than stellar GPA, to work with him has been an experience of a lifetime and I am forever grateful. His patient mentoring has made all the difference in my success, and has allowed me to culminate my research from undergraduate to graduate within this thesis.

I give special thanks to my committee members Dr. Prakash Vedula and Dr. Wei Sun for their time and effort, both in class lectures and in reviewing my work for my thesis defense.

I would also like to acknowledge Professors Steven Fowler, James Gilbert, and Angela Papagolos for their charismatic teaching styles and for fostering a stimulating learning environment at Rose State College.

Finally, I would like to thank my parents, Laura & Jeffery Blosser, for their unwavering support and encouragement throughout my entire academic career. Their belief in me has been a constant source of motivation, and I am deeply grateful for their sacrifices and love.

Like the Ouroboros, research into asteroids is an endless process of modeling and approximation to ensure success on missions. Scanning the stars for these distant harbingers of death, the inevitable fact comes to light of their value. Our civilization looks to utilize their resource, mined & collected, to give life; sustaining the human species into the modern era. From what takes life, gives life.

Contents

List of Figures

List of Tables

Dedicated to the loving memory of my best friend forever. Loki, you were there for everything and you meant more to me than the world. You will always be my sweet baby boy, I miss you everyday.
I love you so much.

Chapter 1

Introduction

1.1 A Brief History on Gravity

Gravitational forces were first defined by Sir Isaac Newton within the third book of his *Principia Mathmatica*, “the weight of either sphere towards the other will be reciprocally as the square of the distance between the centers” (Newton, 1687). Thus, the force of gravity between two bodies is proportional to the masses multiplied and the inverse square of the distance. Mathematically, this takes the form $F \propto \frac{m_1 m_2}{r^2}$, where m_1 and m_2 represent the masses of each sphere or planet, and the distance between the centers is given by r. However, this leaves out the Newtonian gravitational constant, popularly known as Big "G".

It was not until the French physicists Cornu and Baille that this constant was added to Newton’s formulation for gravity in 1873 (Haug, 2022). It would then take Cavendish’s experiment for measuring Earth’s density in 1798, to be reexamined before they discovered that his torsion balance was capable of measuring Big "G" (Haug, 2022). Today modern apparatuses have measured this constant to be $G = 6.67430 \times 10^{-20}\ \frac{km^3}{kg \cdot s^2}$ [1].

In his appending of the *Principia Mathmatica*, Newton stated "hypothese non fingo" in regards as to why the force of any mass lay concentrated at the center (Newton, 1729). This meant that he formed no hypothese, or did not feign any understanding as to why the forces of gravity acted as in such a way. However, this fundamental formulation yielded what we currently know as the point approximation for gravity, where forces are defined at the center of any celestial body. The point approximation takes the modern form of Newton’s force of gravity as $F = G\frac{m_1 m_2}{r^2}$, and is the heart of the Two-Body problem.

Earth and many bodies within our solar system, from Jupiter to the Sun, can all be approximated as point masses for ease of calculation, especially when dealing with full solar system simulations. This approximation is valid to an extent, yet once the task to orbit a satellite around Earth or any other target the point mass is not an ideal gravitational representation. For Earth, we continue research into the gravitational

[1] https://www.physics.nist.gov/cgi-bin/cuu/Value?bg

gradient for refined station keeping of satellites is a continued endeavor. This includes missions such as the Gravity Recovery and Climate Experiment (GRACE) [2]. Or the latest endeavour to place a Quantum sensor into orbit, known as the Quantum Gravity Gradiometer Pathfinder (QGGPf), it will be capable of monitor the ever changing mass distribution of Earth due to geological processes. This is done by use of a gravity gradiometer which utilizes test masses that are free falling and measures the variations in acceleration between them in various positions to test the differences in gravitational forces (Jet Propulsion Laboratory, California Institute of Technology, 2025). These missions are capable of measuring the gravitational field to a high degree of accuracy, allowing for better orbital predictions and station keeping.

1.2 Modeling for Irregular Gravitational Fields of Small Bodies

Asteroids, along with comets and other similar small bodies, pose an even greater challenge due to both mass and geometric shape. Many asteroids have irregular shapes, causing the point mass approximation to only be useful at a distance. Once within the Sphere of Influence (SOI) of an asteroid, new methods of approximating its gravitational field must be utilized to even be able to orbit the asteroid let alone orbit in an optimal manner. The SOI is defined as the region around a celestial body where its gravitational influence is dominant over that of a more massive body it orbits such as the Sun (Bate, 2020). Thus, when en route to an asteroid the Sun's gravity is the dominant force and the asteroid can be assumed as a point mass, yet once within the SOI the asteroids gravity is the dominant gravity attractor. Unlike the Earth, which can be orbited with simpler point mass approximations, if these approximations were used on asteroid dynamics within its SOI, the results could be catastrophic collision or escape trajectories that would send multi-million dollar spacecraft careening into deep space.

Spherical harmonics utilizes gravitational coefficients known as C_{20}, commonly referred to as J_2, and C_{22} which describe the perturbations due to oblateness and equatorial ellipticity respectively (Scheeres, 2012). These coefficients, especially the J_2, are commonly used to describe the perturbations in Earth's orbit along with the point mass approximation as added terms. Yet, this still remains as an approximation and not a detailed gravitational model. Furthermore, for asteroids with highly irregular shapes like (216) Kleopatra [3] and (486958) Arrokoth[4], shown in Figure 1.1, spherical harmonics

[2]https://www.jpl.nasa.gov/missions/gravity-recovery-and-climate-experiment-grace/
[3]https://www.vaticanobservatory.org/sacred-space-astronomy/in-the-sky-this-week-june-16-2020/
[4]https://exploredeepspace.com/wp-content/uploads/2020/06/arrokoth-remnant.jpg

can't be applied as there is viable way to define a spheroid shape around these bodies. This spheroid's shape defines the coefficients of spherical harmonics and is the basis of this method (Scheeres, 2012). For certain asteroids with less irregular shapes spherical harmonics can be applied, yet this method is limited by how spherical in nature the asteroid is.

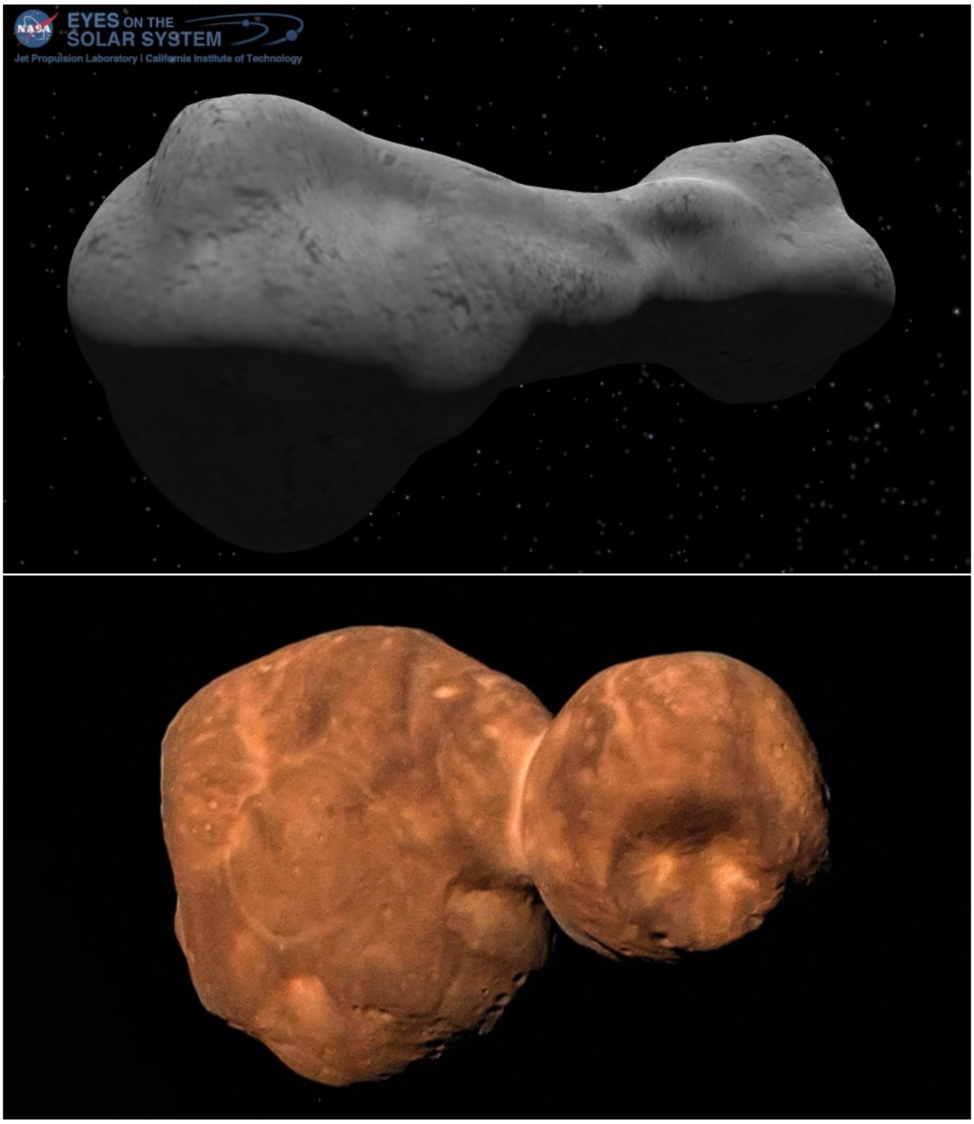

FIGURE 1.1: irregularly shaped asteroids: Kleopatra (top) Arrokoth (bottom).

Most modern day modeling of asteroids utilizes radar and light curve inversion based data, creating two dimensional echos of distant asteroid shapes, which are utilized to generate polyhedron shape models (Benner, n.d.). Polyhedron gravity models, such as Tsoulis, calculate the gravitational forces directly from these polyhedron shape models using line integral analytical formulations (Tsoulis and Gavriilidou, 2021). However, the polyhedron gravity model can be costly when it comes to computation power required due to the lengthy line integrals (Scheeres, 2012). This is especially true for irregularly shaped bodies like asteroids, where the complexity of the shape can lead to significant increases in computational time and resources. As a result, while polyhedron gravity models can provide more accurate gravitational field representations, they may not always be practical for real-time applications or missions requiring rapid calculations. However, the polyhedron shape models themselves can be quite useful with regards to other methods of modeling.

Databases such as the Database of Asteroid Models from Inversion Techniques (DAMIT) contain these polyhedron shape models of thousands of asteroids in our solar system (Ďurech, Sidorin, and Kaasalainen, 2010). This work in specific utilized the database created by Greg Frieger known as the 3D Asteroid Catalogue (Frieger, accessed 2025). This catalogue utilized the DAMIT database to create a more organized catalogue of asteroid polyhedron shape models. Most polyhedron models are approximations at best and several shape models can be found for a singular asteroid based of these distant images. The only high fidelity shape models are those that have been visited by spacecraft, such as (101955) Bennu which was the main focus of the OSIRIS-REx mission (Nolan et al., 2013). This brings us to the main focus of why modeling accurately and efficiently is critical, as the asteroid is remodeled on mission approach.

From afar we can only approximate the shape and composition of any asteroid and thus accurate and efficient remodeling of the shape and gravitational field is essential to minimize time taken in high altitude orbits around asteroids before descending closer. For this reason, asteroids missions can be seen as an Ouroboros problem, the snake eating its own tail, as we make initial approximations based on limited data which are then refined as more information becomes available during the mission.

Here, the core of this study the MASCON model is introduced. This method of modeling can define complex geometric shapes as individual point masses that form a particle cloud. It is this cloud of particles, representing the irregular shape of an asteroid, that is used to approximate the gravitational forces. This is a far more ideal approximation than that of the point mass, especially when conducting space missions near or distant asteroids. It is more computationally efficient than the polyhedron model, and is a more accurate gravitational model than the spherical harmonics, thus creating a balance between accuracy and efficiency.

The use of MASCON dates back to Muller and Sjogren, where the term was used for mass concentration near the Lunar surface in the late 60's (Muller and Sjogren, 1968). Since then it has been used in numerous modeling techniques from the Earth and Moon to asteroids (Antoni, 2022). Recently it has been used to model and compute initial spacecraft dynamics for the asteroid (99942) Apophis (Aljbaae et al., 2020). Apophis, named for the Egyptian serpent god fabled to bring eternal darkness, made headlines as initial observations suggested possible impacts in 2029, and again in 2036, only to be recently ruled out for any impact risk for at least 100 years (The Planetary Society, 2025).

At its size Apophis could live up to its given name, as it is taller than the empire state building on its shortest axis, and could reign destruction if it were to impact Earth (The Planetary Society, 2025). Luckily it remains only as a distant threat in time, yet still draws our attention as a potentially hazardous asteroid (PHA). Thus, OSIRIS-REx has been given a new mission to rendezvous with Apophis as its mission to bennu is completed, renamed OSIRIS-APEX it is now laying in wait for Apophis' visit to Earth (NASA Science, 2024). On April 13^{th} Apophis will make its closest approach to Earth at a distance of $30,600km$, or a tenth the distance of the Moon to Earth, and can be seen by the naked eye streaking across our sky (The Planetary Society, 2025). OSIRIS-APEX will make detailed observations of Apophis during this close approach, gathering valuable data on its surface composition and structure, allowing for precise models to be created for future missions.

1.3 Outline of Thesis

First the method of creating MASCON models is discussed in detail, along with creating simulations for the models in Python. Next the MASCON model created in this work is verified with previous works on (99942) Apophis, before being applied to the asteroid 1950DA. The verification is done through a series of simulations recreating results from previous works on Apophis (Aljbaae et al., 2020). Simulations are then carried out for 1950DA along with analysis by Poincaré surface of sections, outlining the orbital dynamics of small bodies around the asteroid. This defines the regions of chaos and stability allowing for possible periodic and resonant orbits to be identified. Following this the dynamics around the asteroid 1950DA are analyzed for preliminary mission design including: the identification of equilibrium points and their stability, defining capture and scanning orbits utilizing control laws, and potential landing sites along with ΔV expenditures for capture to landing. The study also examines the possibilities of utilizing machine learning to reduce the MASCON model and its computational burden during the simulations. Finally, the study looks to examine ring formation dynamics around 1950DA, simulating surface particles ejected from the asteroid to see if they form a ring structure.

Chapter 2

Asteroid Modeling

2.1 Creating a MASCON Model of Asteroids

Mass Concentrations (MASCON) are a way of mathematically describing an irregular geometric shape by defining its shape by mass. The MASCON model is derived from radar imaging and light curve inversion data which derive a complex polyhedral shape model. These derived polyhedron shapes define our current asteroid models, and are available on most public databases. The main data format of these polyhedron shape models is Alias Waveform Format (OBJ) which is widely used as it is a simplified structure of vertex and face coordinate data. This essential vertex and face data contained within the OBJ file is used to detail the polyhedron shape. Each set of vertices is specified by a face index, these faces represents the outer side of a tetrahedron or 3-Dimensional triangle with three vertices for each face. These tetrahedrons are what comprise the total polyhedron shape, with the polyhedron shape's center serving as the tip or 4^{th} vertex for each tetrahedron. This center is referred to as the Polyhedron center of mass (CM), correlating to the asteroid's center of mass.

The MASCON are derived by utilizing the analytical method for locating the CM for a tetrahedron, also referred to as weighted sums. This takes the vertices $v_1(x_1, y_1, z_1)$, $v_2(x_2, y_2, z_2)$, and $v_3(x_3, y_3, z_3)$; along with the point $P_{CM}(x_p, y_p, z_p)$ that defines the polyhedron's CM. This weighted sum is shown in Equation (2.1) below, with the total number of calculated CMs being equal to the number of tetrahedrons.

$$T_{CM} = \left(\frac{(x_1 + x_2 + x_3 + x_p)}{4}, \frac{(y_1 + y_2 + y_3 + y_p)}{4}, \frac{(z_1 + z_2 + z_3 + z_p)}{4} \right) \tag{2.1}$$

Figure 2.1 shows a diagram of a tetrahedron formed by the vertices and the polyhedron CM, and how the MASCON is defined at the tetrahedron's CM location T_{CM}. We can see that the vertices create an outside surface that serves as the face that defines the surface of the polyhedron shape with each tetrahedron connected by shared vertices and sides. This is why the face index for the vertices is crucial for defining the model as a single vertex can be related to multiple tetrahedrons.

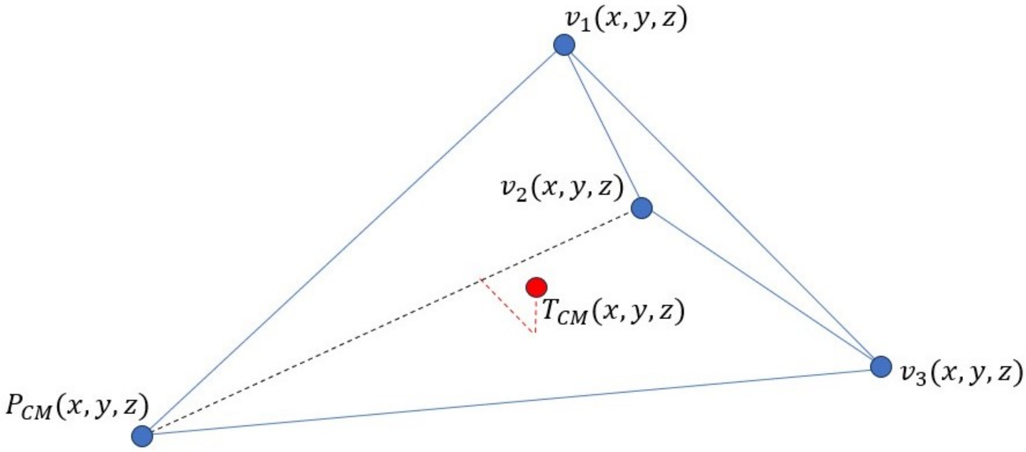

FIGURE 2.1: Tetrahedron representation for calculating the center of mass.

The tetrahedron count is proportional to the face count within the OBJ file of the asteroids shape, which is thus proportional to the generated CM calculated for each MASCON model. The face data itself acts as the indices for the vertices, as stated previously, and is a crucial step for understanding the OBJ file format. One useful software is `volInt.c` which is used to calculate the center of mass of the polyhedron shape, located on it's respective GitHub repository (Mirtich, 1996). Another method is the Python package `trimesh`, which can be installed via `pip`. Both of the softwares can also calculate the volume, so to verify volumetric calculations, the triple scaler product can be used to calculate the volume of each tetrahedron and subsequently the polyhedron shape. This calculation is shown in Equation (2.2) takes each vector X, Y, Z drawn by the vertices of the tetrahedron and polyhedron CM, and calculates the volume. The tetrahedron calculations are then summed to calculate the total volume of the shape model, verifying the calculations performed by `volInt.c` and `trimesh`. These software packages were tested in development to ensure the accuracy of the volume and polyhedron CM calculations. As the results were near identical either software can be used, yet as the `volInt.c` is more widely used, it was chosen for this thesis Aljbaae et al., 2020.

$$V = \frac{1}{6}(u \times v \cdot w) = \frac{1}{6}\begin{vmatrix} X_1 & Y_1 & Z_1 \\ X_2 & Y_2 & Z_2 \\ X_3 & Y_3 & Z_3 \end{vmatrix} \tag{2.2}$$

To keep inline with industry standards, the CM calculations utilize the polyhedron CM calculated using `volInt.c` which aided in generating the MASCON model, while the volume calculations are verified using both software packages.

2.1.1 Scaling the MASCON Model

One key step in creating the MASCON model is scaling the model to size. This is due to the fact that the vertices within the OBJ file are non-dimensional, and thus the volume of the shape is also non-dimensional. Thus, a key aspect of the modeling process is determining the appropriate scaling factor to apply to the non-dimensional vertices in order to obtain a realistic representation of the asteroid's shape and volume. This scaling factor is defined as γ, and is utilized in the calculation of the gravitational parameter for each MASCON as well as scaling the polyhedron shape mesh defined by the OBJ file.

From the tetrahedron volume calculations in Equation (2.2), along with the scaling factor γ the gravitational parameter for each MASCON can be calculated. This is what defines the gravitational influence of each MASCON on an orbiting particle. We define μ_i as the calculated gravitational parameter for each m_i MASCON, calculated using Equation (2.3), where M_i is the mass of the i^{th} MASCON. This mass is correlated to the volume of each tetrahedron V_i, and the density ρ of the asteroid.

$$\mu_i = GM_i\gamma = G(\rho V_i \gamma) \tag{2.3}$$

Taking Newton's gravitational constant to be $G = 6.67430 \times 10^{-20} \frac{km^3}{kg \cdot s^2}$, as previously stated. Equation (2.3) introduces the scaling factor γ to tie the non-dimensionality of the asteroid's shape model, in the OBJ file, to the volume of each tetrahedron. This gives dimensional units to the model and gives room to remodel the asteroid as new data is taken to solidify key parameters. Equation 2.4 defines the percent difference between the volume of the polyhedron shape model $V_{polyhedron}$ and the accepted volume $V_{accepted}$, with the volume of the polyhedron in non-dimensional units and requiring a scaling factor γ to convert to dimensional units.

$$\text{Percent Difference} = \frac{V_{polyhedron} - V_{accepted}}{V_{accepted}} \tag{2.4}$$

This percent difference is then used to calculate the scaling factor γ in Equation (2.3), where an iterative process is carried out until the set tolerance of 1×10^{-9} is reached. The tolerance is used to ensure $V_{polyhedron}$ is almost identical to $V_{accepted}$ utilizing the function `np.isclose` [1]. A variable $\Delta\gamma$ is defined to be the change in scaling factor between iterations, this is monitored and adjusted using `if` statements to be in a range of $0.1 \geq \Delta\gamma \geq 1 \times 10^{-10}$. Each iteration is monitored and adjusts γ by $\Delta\gamma$ until the tolerance is met. Utilizing an `if/elif` statement, $\Delta\gamma$ is added or subtracted if the polyhedron volume is below or above the accepted volume, respectively. The final

[1]https://numpy.org/doc/stable/index.html

scaling factor γ is then used to scale the volume of each tetrahedron V_i in Equation (2.3) to calculate the gravitational parameter μ_i for each MASCON. This iterative process was then carried out again, using $\Delta\rho$ to verify the model's against the accepted density ρ. This second iterative process also uses a percent difference and helps validate the value of γ calculated in the first iterative process.

2.2 MASCON-System

The system defined is a body-fixed rotating frame, with an exterior particle orbiting the asteroid. The asteroid model is comprised of MASCON, which represents the CM of each tetrahedron of the polyhedron shape model for the asteroid as shown in Figure 2.1. The analysis of the gravitational potential of the MASCON model is derived from the theory of the potential in which we treat it as an N-body problem (MacMillan, 1958a). The attraction of an m_i particle system on a single m_0 particle can be described as the summation of forces, or vectors describing the attractions, of the m_i particles; for $i = 1, 2, \ldots, N$. For this system, the external orbiting particle is defined as the m_0 mass being subjected to perturbative gravitational forces by the m_i particle cloud defining the model of the asteroid. Here, the term N represents the number of center of masses within the MASCON model. The gravitational potential is shown below in Equation (2.7), along with the derivatives in Equation (2.6) which describes the acceleration imparted to the orbiting particle due to the asteroid's gravitational influence.

$$U = \sum_{i=1}^{N} \frac{\mu_i}{r_i} \tag{2.5}$$

$$U_x = -\sum_{i=1}^{N} \frac{\mu_i r_{x_i}}{r_i^3} \qquad U_y = -\sum_{i=1}^{N} \frac{\mu_i r_{y_i}}{r_i^3} \qquad U_z = -\sum_{i=1}^{N} \frac{\mu_i r_{z_i}}{r_i^3} \tag{2.6}$$

With the following relations:

- $R_i(x, y, z) = T_{CM}(x, y, z) - P_{CM}(x, y, z)$
- $x = x_p - R_i(x), y = y_p - R_i(y), z = z_p - R_i(z)$
- $r_i = \sqrt{x_i^2 + y_i^2 + z_i^2}$

Where the external particle's position is defined by the coordinates (x_p, y_p, z_p), while the position of each MASCON is defined by the coordinates $T_{CM}(x, y, z)$ and the polyhedron CM is defined by $P_{CM}(x, y, z)$. The equations above reflect the direction of each gravitational force vector of the particles m_i acting upon m_0 within our given space (MacMillan, 1958b). These direction cosines are also reflected within Equation (2.8) through Equation (2.13). These reflections show the influence each particle within the m_i mass concentration has upon the external orbiting particle m_0. Figure 2.2 shows a depiction of this N-body system, with the orbiting particle m_0 being influenced by the gravitational forces of each m_i particle.

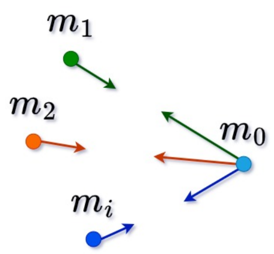

FIGURE 2.2: Gravitational potential of a particle cloud acting upon an orbiting external particle with mass m_0.

With this we are able to define the gravitational potential of a particle cloud acting upon an orbiting external particle with mass m_0 in Equation (2.7). Here we note that μ_i defines the gravitational parameter for each individual tetrahedron as, $\mu_i = Gm_i$, with Newton's gravitational constant taken to be approximately 6.67430×10^{-20} km^3/kgs^2.

$$U = \sum_{i=1}^{N} \frac{\mu_i}{r_i} \tag{2.7}$$

Following this equation, are the gradients of the potential in Cartesian coordinates.

$$U_x = -\sum_{i=1}^{N} \frac{\mu_i(x - x_i)}{r_i^3} \tag{2.8}$$

$$U_y = -\sum_{i=1}^{N} \frac{\mu_i(y - y_i)}{r_i^3} \tag{2.9}$$

$$U_z = -\sum_{i=1}^{N} \frac{\mu_i(z - z_i)}{r_i^3} \tag{2.10}$$

The Hessian of the gravitational potential, utilized for calculating the equilibrium points of the systems, is as follows (Aljbaae et al., 2016).

$$U_{xx} = -\sum_{i=1}^{N} \left(-\frac{\mu_i}{r_i^3} + \frac{3\mu_i(x - x_i)^2}{r_i^5} \right) \tag{2.11}$$

$$U_{yy} = -\sum_{i=1}^{N}\left(-\frac{\mu_i}{r_i^3} + \frac{3\mu_i(y-y_i)^2}{r_i^5}\right) \tag{2.12}$$

$$U_{zz} = -\sum_{i=1}^{N}\left(-\frac{\mu_i}{r_i^3} + \frac{3\mu_i(z-z_i)^2}{r_i^5}\right) \tag{2.13}$$

$$U_{xy} = -\sum_{i=1}^{N}\left(\frac{3\mu_i(x-x_i)(y-y_i)}{r_i^5}\right) \tag{2.14}$$

Where for remaining Hessian components are found with Equation (2.14) & defining $x \neq y \neq z$.

2.2.1 Equations of Motion for a Particle in a Rotating Frame

The main system for placing a particle in motion orbiting the MASCON model is the body-fixed rotating frame, with the asteroid rotating at a constant angular velocity ω. Equation (2.15) shows the equations of motion in the rotating frame, with both the Coriolis and centrifugal forces present, along with the potential given by the MASCON model U_r (Aljbaae et al., 2020).

$$\ddot{\vec{r}} = -2\vec{\Omega} \times \dot{\vec{r}} - \vec{\Omega} \times (\vec{\Omega} \times \vec{r}) + U_r \tag{2.15}$$

Within this work we assume the rotation of the asteroid is about the z-axis, thus $\vec{\Omega} = [0, 0, \omega]$. This is a fair and accurate assumption until closer observation of the target is undertaken, usually by sending a spacecraft to visit the asteroid or closer observations are performed. This reduces the equations of motion to the following form in Equation (2.16). Here, the Coriolis and centrifugal forces are present within the XY-plane, while the z-axis only has the gravitational influence of the MASCON model.

$$\ddot{x} = \omega^2 x + \omega\dot{y} + U_x \tag{2.16}$$

$$\ddot{y} = \omega^2 y - \omega\dot{x} + U_y \tag{2.17}$$

$$\ddot{z} = U_z \tag{2.18}$$

Equation 2.16 shows U_x, U_y, and U_z as the gradients of the gravitational potential defined in Equation (2.8) through Equation (2.10), and represents the gravitational influence of the MASCON model U_r.

2.2.2 Hamiltonian Mechanics for Orbiting Particles

Near small-bodies like asteroids classical orbital elements fail as the irregular gravitational fields of asteroids are highly perturbed and classified as non-Keplerian environments. Thus, Keplerian elements, such as the classical orbital elements, become numerically unstable as they violate the assumptions that define Keplerian motion and cause singularities when calculating the elements (Scheeres, 2012). This makes the ideal choice for the mechanics to be Hamiltonian, in place of the classical orbital elements, as they are not violated. Using the following equation for Hamiltonian energy we solve for the velocity of our particle using the assumption that we are setting off from the y-axis in the positive x-direction with a positive $\dot{x}$ velocity. Thus we assume that $\dot{y} = \dot{z} = x = z = 0$ within Equation (2.19), and solve for the $\dot{x}$ velocity as shown in Equation (2.20) to set out initial conditions. This assumption is made as the particle is being aimed to allow for the Poincaré Section framework to be applied for the analysis and classification of the orbital trajectories (Aljbaae et al., 2020).

$$H = \frac{1}{2}(\dot{x}^2 + \dot{y}^2 + \dot{z}^2) - \frac{1}{2}\omega^2(x^2 + y^2) - U \tag{2.19}$$

$$\dot{x} = \sqrt{2H + \omega^2 y_o^2 + 2U}. \tag{2.20}$$

where we define U as the pseudo potential from Equation (2.5), the diagram in Figure 2.3 depicts our orbit with these initial conditions given.

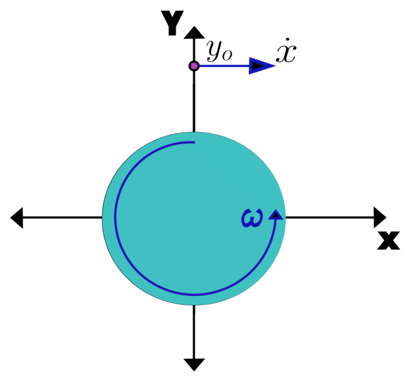

FIGURE 2.3: Depiction of initial orbital orientation. We have the asteroid rotating in a prograde motion relative to the solar system, and the particle orbiting the asteroid in a retrograde motion.

2.3 Analysis of Trajectories & Poincaré Surface of Section

Orbital trajectories can exhibit many different dynamic behaviors, each with its own classification. In this context, we define the essential solution types relevant to the Circular Restricted Three-Body Problem (CR3BP). Note that these are not orbital shapes; rather, they describe categories of dynamical solutions within the CR3BP framework. The primary solution types are:

1. Periodic Orbit: This motion is the ideal scenario, in which the motion of the particle or spacecraft returns to its exact initial condition or position after $N \cdot T$ where T is the period of the system. If $N = 1$ it is referred to as a periodic orbit of period 1, $N = 2$ is a periodic orbit of period 2 and so on (Moehlis, Josic, and Shea-Brown, 2006). A perfect solution would be up to 8 decimal places of precision.

2. Quasi-Periodic Orbit: This motion is far more common, as this motion is bounded in a torus shape, and does classify as bounded motion (Broer, Huitema, and Sevryuk, 2009). However, this is not as periodic and may never return to it's initial condition. Quasi-periodic orbits appear in the vicinity of periodic orbits, they form a torus shape around the periodic orbit in phase space (Murray and Dermott, 1999).

3. Equilibrium Points: These points are defined as the location in which the gravitational and perturbations balance out, allowing for a stationary point in the rotating frame. These points are found at places where the velocity is zero within the equations that define the particle's energy (Aljbaae et al., 2016).

4. Chaotic Orbits: These orbits are characterized by their sensitivity to initial conditions, leading to unpredictable and complex behavior over time. Chaotic orbits can arise from various factors, including gravitational interactions and perturbations from other bodies in the system Murray and Dermott, 1999.

There is also the resonant orbit which is a type of periodic orbit that occurs when the orbital period of the particle is a simple fraction of the rotation period of the asteroid. These orbits are of particular interest as they can provide stable paths for spacecraft to orbit the asteroid while minimizing fuel consumption. Resonant orbits can also be used to study the dynamics of the asteroid's rotation and its effect on the surrounding environment (Scheeres, 2012).

A Poincaré surface of section is a method of reducing the dimensionality of a system's phase space, allowing for the visualization of complex dynamics in a more manageable way. The surface of section is constructed by defining a hyperplane in the phase space, and then recording the points at which the trajectory of the system intersects this hyperplane. This surface of section is shown in Figure 2.4, where x_0 represents the initial condition of the particle, and the next points x_1 and x_2 are recorded as the trajectory intersects the defined hyperplane constructing the Poincaré map. The Poincaré map of the surface of section represents both position and velocity with respect to a defined axis crossing. Thus, this axis crossing is where the hyperplane, or surface of section, is constructed (Scheeres, 2012).

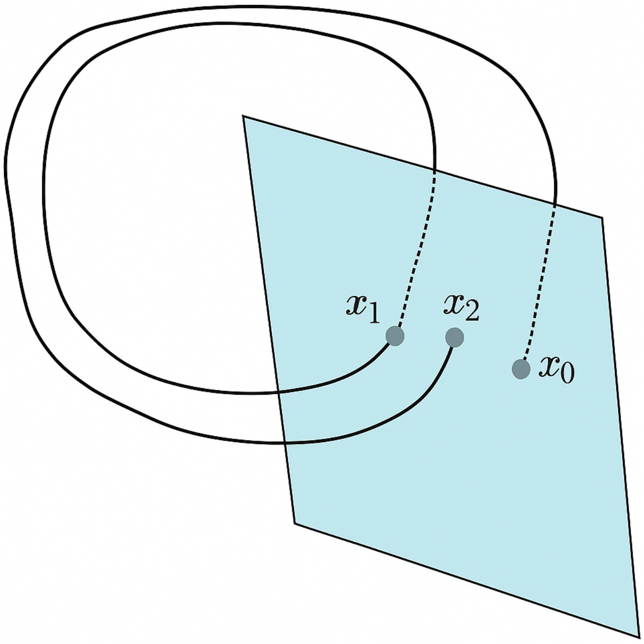

FIGURE 2.4: Depiction of Poincaré surface of section construction. This diagram was created with Generative AI, using a diagram from Dr. Scheeres *Orbital Motion in Strongly Perturbed Environments* (Scheeres, 2012).

Reading the Poincaré surface of section is done by analyzing the shape of the section. The portion where we see a cluster of random points, defines chaotic motion, where the particle is not in a stable orbit. The portion where we see a dense line of points, forming circles or elliptical shapes, defines quasi-periodic motion. The portion where we see a blank spots inside the circular or elliptical shapes within the section, defines the torus shaped trajectories, and separates the Quasi-periodic motion from the periodic motion. The center of these shapes give the initial position and velocity that would lead to a periodic orbit. These blank spots are refereed to as islands of stability, within the center of the island is the location of a periodic orbit. Thus, by analyzing the Poincaré surface of section, we can classify the motion of the particle based on its trajectory. If the points form a dense circle or elliptical shape, it is classified as quasi-periodic motion, if the points are scattered randomly, it is classified as chaotic motion, and if there is an island of stability present, the center of the island is classified as a periodic orbit.

For this work, the Poincaré surface of section is constructed by defining the hyperplane at the $x = 0$ plane, choosing this hyperplane due to the asteroid's symmetry, and recording the points at which the trajectory of the system intersects this hyperplane. This is performed using a sign change detection algorithm, where we define x_i and x_{i+1} as the position of the particle at time t_i and t_{i+1}, respectively. If x_i and x_{i+1} have opposite signs, then the trajectory has crossed the hyperplane. To generate one side of the Poincaré surface of section, we define the additional condition that $x_i > 0$, meaning that the particle is moving in the positive x-direction as it crosses the hyperplane. This also ensures that the particle makes one full revolution around the asteroid before crossing the defined hyperplane. Removing this secondary condition generates a two sided Poincaré surface of section with the asteroid, or any target body, at the center of the Poincaré map.

For some works, such as the Chaotic Regions of the Inner Solar System - Chaotic Regions of the Outer Solar System project (CRISS-CROSS), the exact crossing of the hyperplane is carried out utilizing a Newton-Raphson method on the trajectories (Winter and Murray, 1994). This method is used to find the precise point of the hyperplane crossing defined by zero on the chosen axis, yet can be difficult to implement. Thus for this work, an averaging of states is utilized once the sign change algorithm detects a hyperplane crossing on the x-axis. Equation 2.21 shows the averaging of the states at t_i and t_{i+1}, where y_{cross} and $\dot{y}_{cross}$ are the position and velocity of the particle being recorded at the hyperplane crossing. This sign change algorithm and averaging of states is utilized in place of the Newton-Raphson method.

$$y_{cross} = \frac{y_i + y_{i+1}}{2} \quad \& \quad \dot{y}_{cross} = \frac{\dot{y}_i + \dot{y}_{i+1}}{2} \tag{2.21}$$

This method is nearly as accurate as the Newton-Raphson method especially when the integration time step is small, and is significantly faster to compute. This is especially useful when running a large number of simulations, as each simulation can be run on a separate core, significantly reducing the overall computational time.

2.4 Defining the Simulation

To define the simulation, we utilize the python package `scipy.integrate.solve_ivp`, which is a powerful integrating tool for solving Ordinary Differential Equation (ODE) in Python. This package provides several methods of integration, the one utilized for this work is the Dormand-Prince 853 or `DOP853` algorithm which utilizes the Runge-Kutta method of order 8 [1]. This method is a high-order explicit method for solving ordinary

[1]https://docs.scipy.org/doc/scipy/

differential equations, and is particularly well-suited for problems that require high accuracy, such as the CR3BP.

The input to the integrator is the equations of motion defined in Equation (2.16), which are rewritten as a system of first-order ODE. This is done by defining a initial state vector as shown below, where y_0 is the initial position along the y-axis, and $\dot{x}$ is the initial velocity found by Equation (2.20). This is the initial state represented in Figure 2.3, where the particle is set off from the y-axis in the positive x-direction with a positive $\dot{x}$ velocity.

$$Initial\ State = \begin{bmatrix} 0 & y_0 & 0 & \dot{x} & 0 & 0 \end{bmatrix}^T$$

In addition to the three acceleration equations within Equation 2.16, the velocity is defined as the derivative of position, defining the full state vector as six first-order ODEs, which is then integrated over time using `solve_ivp()`. Thus, the output is a vector that is the integrated position and velocity for the given time span of integration:

$$Solution = \begin{bmatrix} x_i & y_i & z_i & \dot{x}_i & \dot{y}_i & \dot{z}_i \end{bmatrix}$$

where i is the time span to the final time t_f in seconds for $i = 1, 2, \ldots, t_f$.

2.4.1 Collision & Escape Events

In order to set conditions for escaping or colliding particles, functions for these limits need to be defined. For the escape limit the Hill's Sphere was utilized, similar to the SOI, it defines the region around a smaller body in which the gravitational attraction of the body dominates over tidal influences of a much larger body such as the Sun. The Hill's Sphere is calculated using Equation 2.22 and derived for the CR3BP framework, unlike the SOI which is a patched-conic approximation (Murray and Dermott, 1999). This Hill's Sphere is then multiplied by a factor of 10, which is common practice for this kind of problem to ensure any particle that escapes does not have a return motion (Aljbaae et al., 2020). Once this particle reaches the distance threshold of this escape limit the simulation is terminated.

$$R_{Hill's} = a(1-e)\left(\frac{M_{target}}{3M_\odot}\right)^{\frac{1}{3}} \tag{2.22}$$

Here we define $M_\odot$ as the mass of the Sun and M_{target} as the mass of the asteroid (Murray and Dermott, 1999). The semi-major axis a and eccentricity e are taken from

National Aeronautics and Space Administration (NASA)'s Jet Propulsion Lab (JPL) Horizons online ephemeris system [2].

To set the limit of collision the python package `trimesh` was utilized for its built in mesh handling capabilities. With this package the OBJ file is loaded and the particle position is monitored relative to the surface of the asteroid defined by the polyhedron shape model scaled to size by γ. There is a finite limit of approximately 2 *meters* set which defines the limit in which a spacecraft will collide with the asteroid inside this limit, allowing for close orbits above the 2 *meter* threshold to still occur. Once the particle reaches this collision limit the simulation is terminated.

2.4.2 Multiprocessing

To decrease the computational time of the simulations, the built in python package `multiprocessing` was utilized. This package allows for the use of multiple Central Processing Unit (CPU) cores on a computer to run simulations in parallel. This is especially useful when running a large number of simulations, as each simulation can be run on a separate core, significantly reducing the overall computational time. This is also a necessary step to utilize The OU Supercomputing Center for Education & Research (OSCER) to its full potential. A single node on OSCER has 64 CPU cores, allowing for 64 simulations to be run in parallel. However there are a few additions that help ensure the simulations run smoothly and efficiently.

One addition in particular is the deletion of the solution once any analysis is performed or the data is saved. This is important as the solution can be quite large, especially for long simulations, and can quickly fill up the Random Access Memory (RAM) of the computer. By deleting the solution once it is no longer needed, the RAM can be freed up and ensure that the simulations continue to run with no errors.

The use of `numba`, specifically the `@njit` decorator, was also implemented to speed up the calculations. This decorator compiles the decorated function to machine code, allowing for faster execution. This is especially useful for functions that are called frequently, such as the equations of motion. By compiling these functions to machine code, the overall computational time can be significantly reduced.

[2]https://ssd.jpl.nasa.gov/horizons/

Chapter 3

MASCON Simulations and Orbital Dynamics

3.1 Checking the Model Using the Well-Known Asteroid (99942) Apophis

The asteroid (99942) Apophis was extensively studied over the years, and there is a rich literature about orbits of particles around this body and the nature of it's spin state Benson et al., 2023. In particular, we can use the work from Aljbaae et al. (2020) to verify the methods and the latest model created within this work. Figure 3.1 shows the OBJ mesh of Apophis, which was retrieved from 3D Asteroid Catalogue (Frieger, accessed 2025).

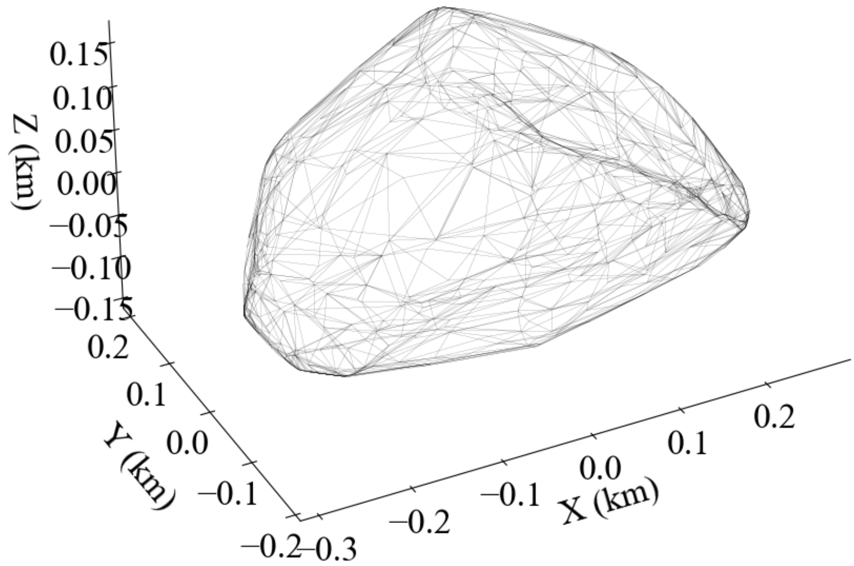

FIGURE 3.1: OBJ mesh of (99942) Apophis.

The shape model of Apophis is comprised of 2024 faces and 1014 vertices defined in the OBJ file. The face count is correlated to the number of CMs within the MASCON model of Apophis shown in Figure 3.2 located in the following section.

3.1.1 Modeling (99942) Apophis with MASCON

The work of Aljbaae et al. (2020) utilized similar methods to create a MASCON model for Apophis and simulate orbits around the asteroid. The scaling factor they found was $\gamma = 0.285 \pm 0.158$, with a Hill sphere radius of 34.0 km multiplied by 10 to ensure no return motion (Aljbaae et al., 2020). Table 3.1 shows the physical parameters used to model Apophis, where γ is the scaling factor calculated within this current work. The mass, density, and accepted volume of Apophis was taken from the works of Aljbaae et al. (2020). The scaling factor calculated within this work was found to be approximately the same, and well within the uncertainty given in the works of Aljbaae et al. (2020).

TABLE 3.1: Physical Parameters of (99942) Apophis from Aljbaae et al. (2020), with the scaling factor for this work.

M	$5.31 \mp 0.9 \times 10^{12}\ kg$
V	$0.03034285\ km^3$
ρ	$1.75 \pm 0.11 \times 10^{12}\ \frac{kg}{km^3}$
μ	$3.5439463859488244e - 09\ \frac{km^3}{s^2}$
γ	0.28481969
Escape limit	$340.0\ km$

The MASCON model of Apophis is shown in Figure 3.2, and is visually identical to that of the model within the works of Aljbaae et al. (2020) serving as our first check of the modeling and software created within this work.
The model is not only comprised of the location for each CM, but also the gravitational parameters for each CM which defines the values of μ_i within Equation 2.7 through 2.14.

3.1.2 Comparing to Other Models

As previously discussed, asteroids like Apophis carry a significant uncertainty about their nature as we view them from afar. Until a target is visited by a spacecraft, taking detailed scans of the surface and analyzing the composition of samples, the model can only be made as an approximation. This is not the end of the mission, as on approach to the asteroid it can be treated as a point mass and any approximate MASCON model is viable. Figure 3.3 reinforces this notion that the asteroid can be approached using approximations, as the relative error between the MASCON model and the point mass converge at a distance of 1.0 km. This relative error, Equation 3.1, is the difference

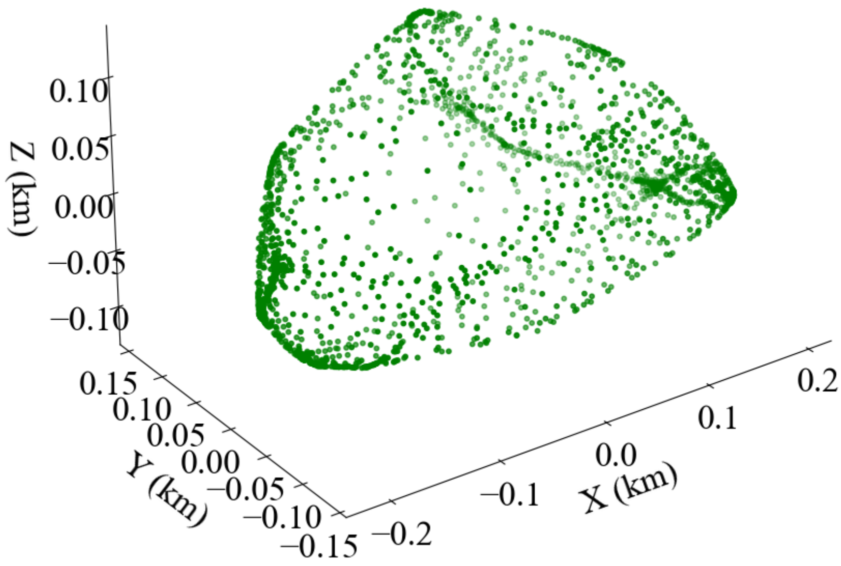

FIGURE 3.2: Recreated model using the MASCON method.

between the gravitational potential calculated using the MASCON model and the point mass approximation, divided by the gravitational potential calculated using the point mass approximation. We also see a comparison with the Tsoulis Polyhedron model, which has been accepted by the industry. For each relative error calculation, we see the convergence at 1.0 *km*, showing that the models are identical with the point mass approximation at this distance. Thus, the MASCON model itself acts similar to the point mass approximation on approach to the asteroid. It is only after arrival that the asteroid can be effectively surveyed for shape and composition, allowing for a more accurate MASCON model to be created. However, the approximated MASCON model is viable for initial orbit calculations and mission planning as well as orbital trajectories beyond the 1.0 *km* mark that are ideal for surveying the surface. Calculations below this mark are still viable as approximations, and after refinement of the model, any close approaches can be optimized to ensure minimal Δv usage, and subsequently mission critical propellant can be saved for additional maneuvers.

$$Relative\ Error = \frac{U_{mascon} - U_{point}}{U_{point}} = \frac{U_{Tsoulis} - U_{point}}{U_{point}} = \frac{U_{mascon} - U_{Tsoulis}}{U_{Tsoulis}} \tag{3.1}$$

This relative error plot shown in Figure 3.3 serves as the second check for the model presented within this work, and is in-line with the relative error between the models and the point mass approximation shown within the work from Aljbaae et al. (2020). This defines a mathematical check on the MASCON model created in this work, and reinforces the visual check for Figure 3.2. Figure 3.3 also shows Tsoulis Polyhedron model, which has been accepted by the industry, and serves as an additional check on the MASCON model (Tsoulis and Petrović, 2001).

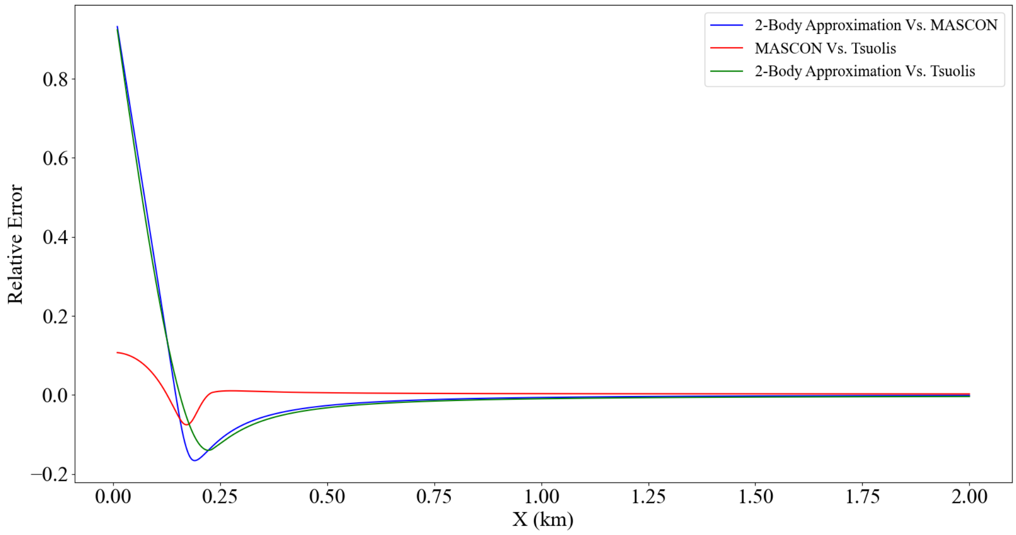

FIGURE 3.3: Relative error in the gravitational potential calculated using: Tsoulis Polyhedron model (Accepted by Industry), MASCON (This work), and the point mass Two-Body approximation.

3.1.3 Poincaré Surface of Section

Defining the set initial of initial conditions that created the previous generated Poincaré surface of sections. Utilizing the defined Hamiltonian mechanics, the energy is held at $H = 1.6 \times 10^{-9} \, \frac{km^2}{s^2}$ and the particle is assigned a linear space of initial positions on the y-axis. This linear space is defined from $y_0 = 0.5 \, km$ to $y_0 = 4.0 \, km$, for every $0.01 \, km$, totaling in 350 simulated orbits. The energy is held constant throughout the simulation as for each section you must hold the energy or position constant in order to vary the other and create a viable Poincaré surface of section. This also reflects the energy and position selection made within the works of Aljbaae et al. (2020) which serves as our check for the Poincaré surface of section as this work is recreated within this thesis. The total time for each simulated orbit was set at 500 *days* with a time step of $\Delta t = 1.0$ *seconds* as previously discussed to ensure the Poincaré surface of section is well-defined with the state averaging over the defined hyperplane. These orbits construct the Poincaré surface of section shown in Figure 3.4 which defines the third and critical check for the MASCON check.

Figure 3.4 shows a similar structure to that of the previous results found within the works of Aljbaae et al. (2020) given the same initial conditions, thus the results agree

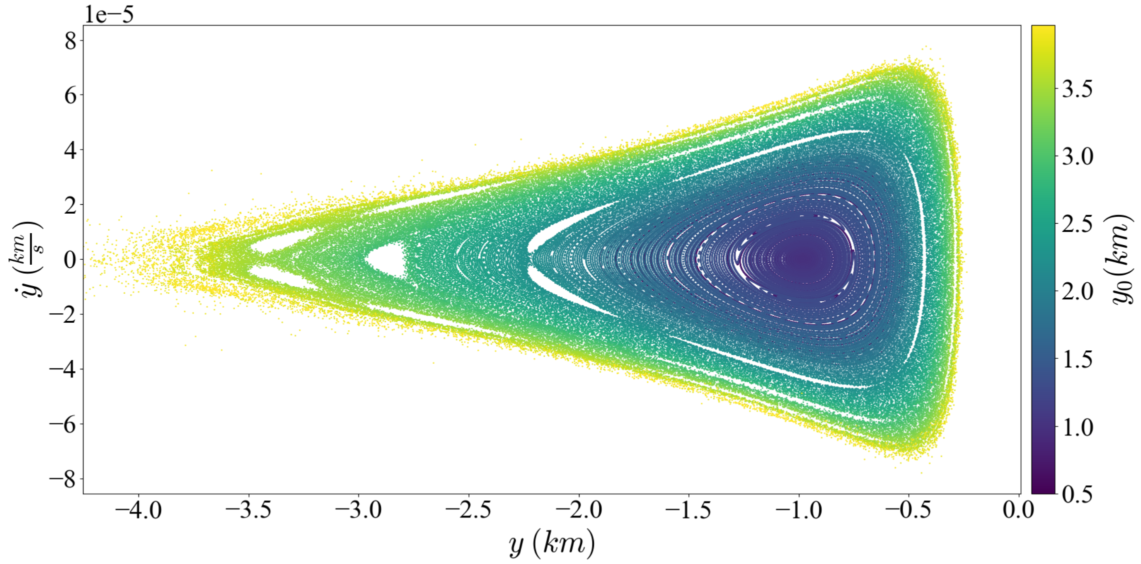

FIGURE 3.4: Poincaré Surface of Section for Apophis. The Hamiltonian energy is $H = 1.6 \times 10^{-9}\ \frac{km^2}{s^2}$, the initial conditions for position are represented in the colorbar as y_0 and reflected in the plot.

with the literature. This visual comparison to surface of sections is what defines the mathematical check for the MASCON model. It can be noted that the current results detail the previous islands of stability almost exactly. Figure 3.5 shows a zoomed in section of the Poincaré surface of section, highlighting the interior structure of the islands of stability. This refined interior structure is not as detailed in the works of Aljbaae et al. (2020), thus this is a new finding that can be explored further in future works. The interior structure of these islands of stability can be used to define the periodic orbits that exist within these islands created by quasi-periodic orbits.

This Poincaré surface of section shown in Figure 3.4 was generated utilizing OSCER with a total of 64 CPU cores running in parallel, and took 1579.876325 *seconds* or approximately 26.33 *minutes* to complete. Additionally an identical run was conducted on a standard computer with an intel i9-9900K, utilizing 5 of the 16 total CPU cores. This calculation took 14677.447896 *seconds* or approximately 4.08 *hours* to complete. Both calculations included the `njit` decorator for the functions that were able to be compiled in machine code with `numba`. Thus, it can be see that a total 350 orbits each simulated for 500 *days* was able to be completed in a reasonable time frame on a standard CPU, and extremely efficiently on a supercomputer such as OSCER.

The other part of the check on the Poincaré surface of section are of the orbital trajectory shapes themselves. Figures 3.6 through 3.9, color coded by their initial position y_0 on the Poincaré surface of section's color-bar, show the orbital trajectory that defined Figure 3.4 and are the same extracted trajectories shown within the works of

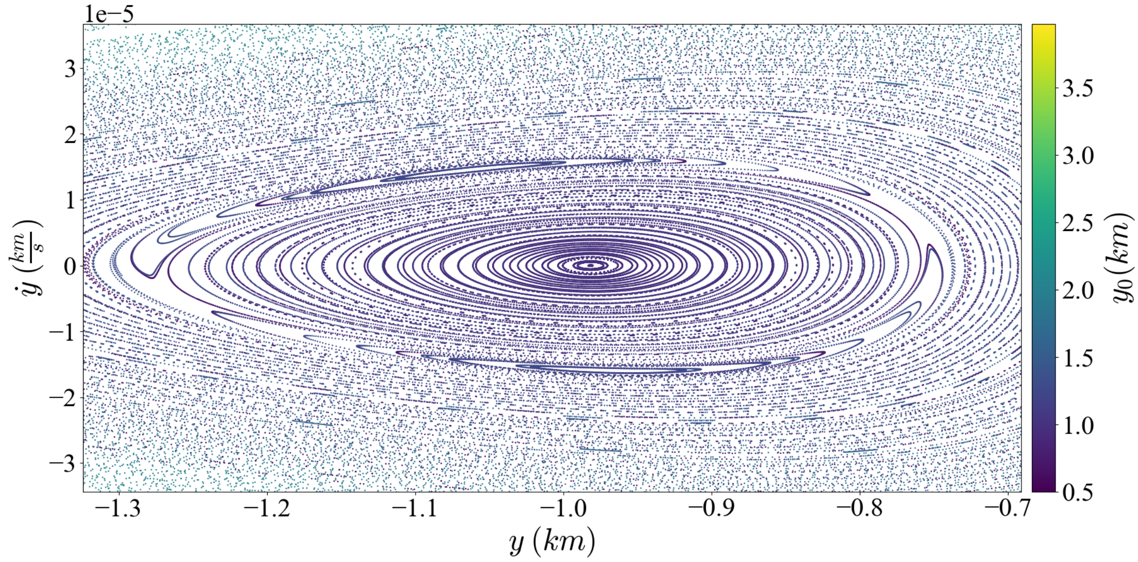

FIGURE 3.5: Interior shape of Poincaré surface of section within Figure 3.4.

Aljbaae et al. (2020). As these trajectory shapes are identical these results agree with the literature and it solidifies the mathematical check on the MASCON model created in this work and the results shown in Figure 3.4 with the additional refinement of the interior structure (Aljbaae et al., 2020).

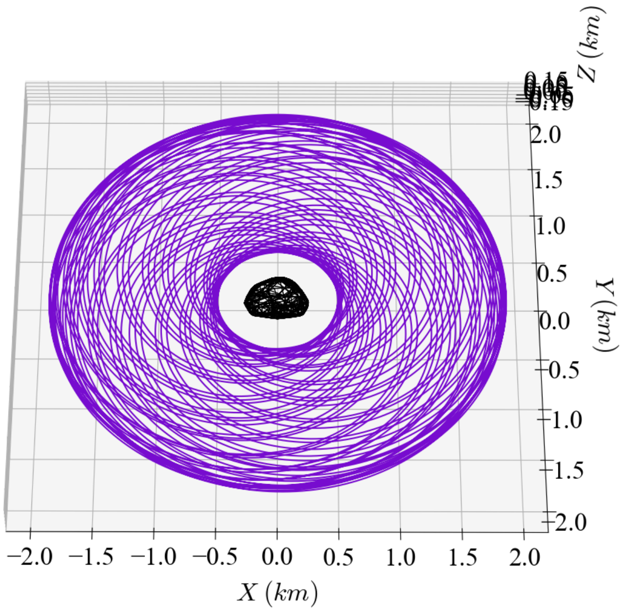

FIGURE 3.6: Apophis trajectory verification for initial condition $y_0 = 0.5\ km$.

The survival map presented within Figure 3.10 is defined by a stability criteria of 60 days in which if the orbits are still viable they are defined as bounded motion which

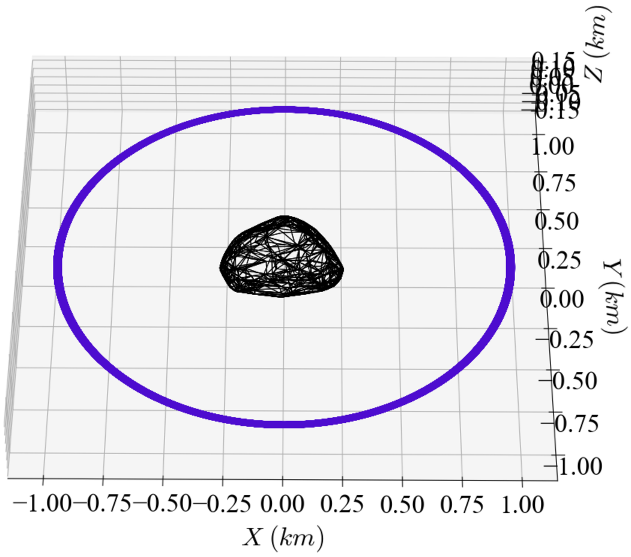

FIGURE 3.7: Apophis trajectory verification for initial condition $y_0 = 1.0\ km$.

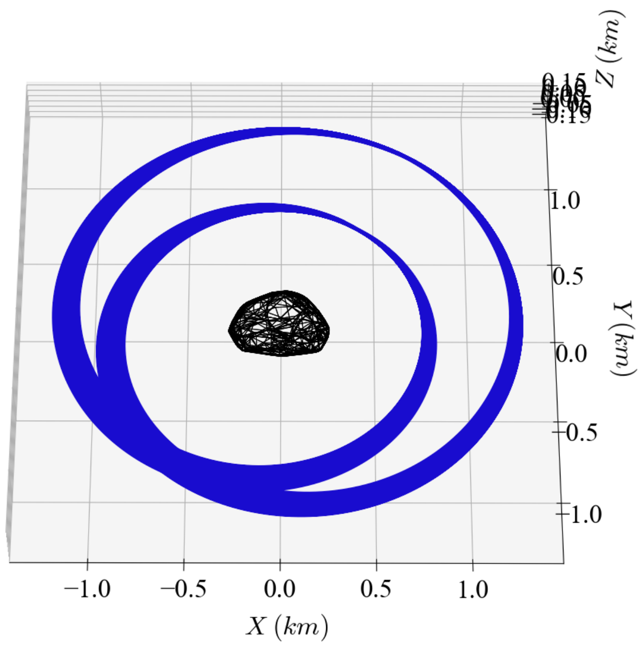

FIGURE 3.8: Apophis trajectory verification for initial condition $y_0 = 1.3\ km$.

is shown in the blue regions. This bounded motion does not mean they are stable, yet do hold for a total of 60 days without any critical event. The survival map also serves as a check on the simulation's critical event definitions of escape and collision in addition to a check on the model. The discrepancies of the collision portion, in red, come from the use of `trimesh` as this was used in place of the Computational Geometry Algorithms Library (CGAL) which was utilized in the works of Aljbaae et al. (2020).

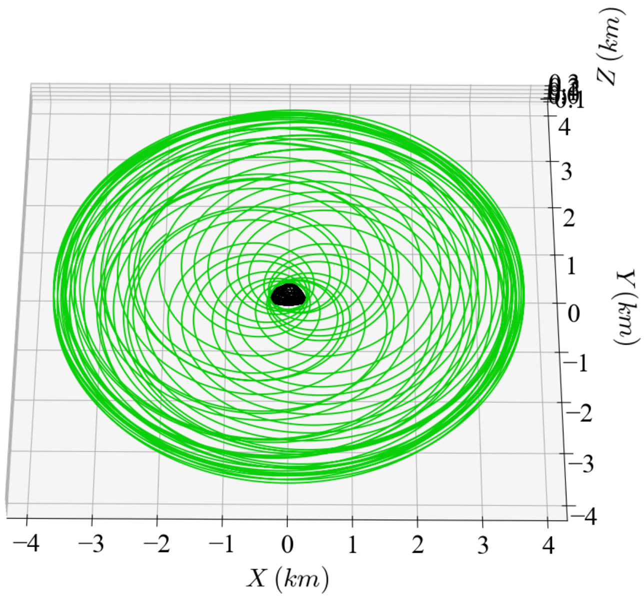

FIGURE 3.9: Apophis trajectory verification for initial condition $y_0 = 3.7\ km$.

The Hamiltonian energy is ranged from $H = 0.1 \times 10^{-9}\ \frac{km^2}{s^2}$ to $H = 5.0 \times 10^{-9}\ \frac{km^2}{s^2}$, with an interval of $0.1 \times 10^{-9}\ \frac{km^2}{s^2}$, and the initial position is ranged from $y_0 = 0.5\ km$ to $y_0 = 10.0\ km$, for every $0.1\ km$, totaling in 4800 simulated orbits.

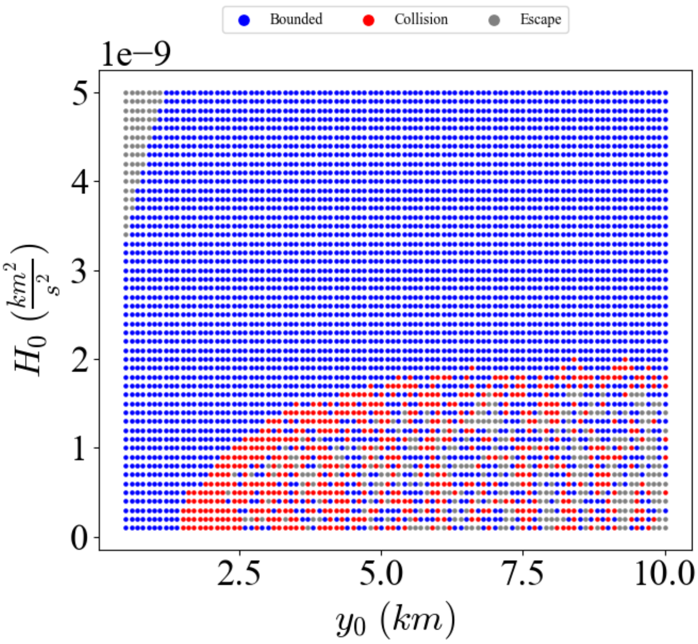

FIGURE 3.10: Survival map of Orbits around Apophis, for a stability criteria of 60 days.

3.2 Orbital Dynamics around (29075) 1950DA

After the validation of the models and software implementation showed in the previous section, this section presents the results for the asteroid (29075) 1950DA, a PHA with a close approach of only 0.05 AU to Earth in 2001, and an impact probability of 2.5×10^{-4} in 2880 (Giorgini et al., 2002; Farnocchia and Chesley, 2014). Solutions for the polyhedron shape models were generated by BUSCH et al. (2007) for both a retrograde and prograde spin, with the understanding that the retrograde model was found to have no potential impact. The prograde polyhedron shape model derived is the one in particular that shows a non-zero impact probability it was the main focus of this study (BUSCH et al., 2007). Since there is no potential impact with the retrograde model, it stands to reason that no mission would need to be designed if it was the correct polyhedron shape model as it would not be PHA in this case. Thus, the prograde model was used to generate a MASCON model and is the one chosen for this work, for the purposes of this study it will be referred to as simply 1950DA.

1950DA is a fast rotating rubble pile also classified as a strength-less asteroid (BUSCH et al., 2007; Pravec and Harris, 2000). As 1950DA rotates in a prograde motion, with $\omega = 2.1216 \pm 0.00004 \frac{rot}{hrs}$, orbiting bodies experience significant centrifugal forces (BUSCH et al., 2007). This rotation is near the theoretical limit for surface cohesion of $\approx 2.2\ hr$ in which beyond this limit rubble pile asteroids will begin to break apart due to the intense rotational forces. Since 1950DA exceeds this rotational period limit by a small margin, it is believed that structural failure may occur as pieces of rubble begin to escape from the surface (Rozitis, MacLennan, and Emery, 2014).

3.2.1 Modeling (29075) 1950DA with MASCON

The most recent analysis of 1950DA has led to a minimum Bulk density of 1.7 ± 0.7 g cm^{-3} and a mass of $2.1 \times 10^{12} \pm 1.1$ kg (Rozitis, MacLennan, and Emery, 2014). During the initial analysis, a rough calculation of the volume was conducted and presented as $0.82\ km^3$ $(\pm 30\%)$ (BUSCH et al., 2007). Table 3.2 shows the parameters used during this work's modeling process of 1950DA. It can be noted that these parameters are well within the large uncertainty given for the accepted values.

Modeling led to a finding of a scaling factor of $\gamma \approx 0.99137$, meaning the non-dimensional OBJ file was close to the correct size leaving the shape model effectively unchanged. The eccentricity of 1950DA is approximately 0.50784 and the semi-major axis is 1.6985 AU [1]. Utilizing the mass of the sun given by the Astronomical Almanac as $M_{\odot} = 1.989 \times 10^{30}\ kg$, and Equation 2.22, the Hill's sphere of 1950DA is calculated to be approximately

[1]https://ssd.jpl.nasa.gov/horizons/

TABLE 3.2: Physical & Orbital Parameters of (29075) 1950DA.

M	$2.1 \times 10^{12}\ kg$
V	$0.797895\ km^3$
ρ	$2.4 \times 10^{12}\ \frac{kg}{km^3}$
μ	$1.27809 \times 10^{-7}\ \frac{km^3}{s^2}$
γ	0.99137
Escape limit	$466.7200\ km$
eccentricity	0.50784
$semi - major\ axis$	$1.6985\ AU$

46.672 km (U.S. Naval Observatory, 2021). Multiplying this by a factor of 10, as previously discussed, gives an escape limit of 466.7200 km which is used as the critical event for escape. The MASCON model of 1950DA is shown in Figure 3.11, and is comprised of 2036 CMs, which is similar to the face count of 2036 within the OBJ file. Within Figure 3.11, the polyhedron shape model is shown as the mesh wireframe, while the MASCON model is shown as the green points inside the wireframe.

3.2.2 Poincaré Surface of Section around Asteroid 1950DA

The survival map shown in Figure 3.12 defines the region of bounded motion around 1950DA. The Hamiltonian energy is ranged from $H = 1.0 \times 10^{-8}\ \frac{km^2}{s^2}$ to $H = 2.0 \times 10^{-6}\ \frac{km^2}{s^2}$, with an interval of $1.0 \times 10^{-8}\ \frac{km^2}{s^2}$, and the initial position is ranged from $y_0 = 0.5\ km$ to $y_0 = 20.0\ km$, for every 0.1 km, totaling in 39200 simulated orbits. This map is similar to that of Apophis, in that is utilizes a stability criteria of 60 days, and only defines bounded motion. The reason this is useful is that it defines the region in which to search for quasi-periodic orbits, and subsequently periodic orbits. The bounded motion region is shown in blue, while the collision orbits are shown in red, and the escape orbits are shown in grey. In Figure 3.12, we can see that there are significant regions of bounded motion for energies with a structure similar to that of Apophis. It also shows that as the energy and distance increases, the region of bounded motion increases as well. From this map the Hamiltonian energies of $H = 3 \times 10^{-7}\ \frac{km^2}{s^2}$ and $H = 4 \times 10^{-7}\ \frac{km^2}{s^2}$ were chosen to generate Poincaré surface of sections, as they show significant bounded motion regions. These Poincaré surface of sections are shown in Figure 3.15 and Figure 3.13 respectively.

Examining the Poincaré surface of sections shown in Figure 3.15 and Figure 3.13, we can see the higher energy of $H = 4 \times 10^{-7}\ \frac{km^2}{s^2}$ shows a larger region of bounded motion, as the chaotic region is not as prevalent with the scattered dots on the exterior representing the chaotic motion. There are signs of resonance orbits up to $y \approx -10.0\ km$ as we see signs of several periodic orbits within each island of stability. This can be seen

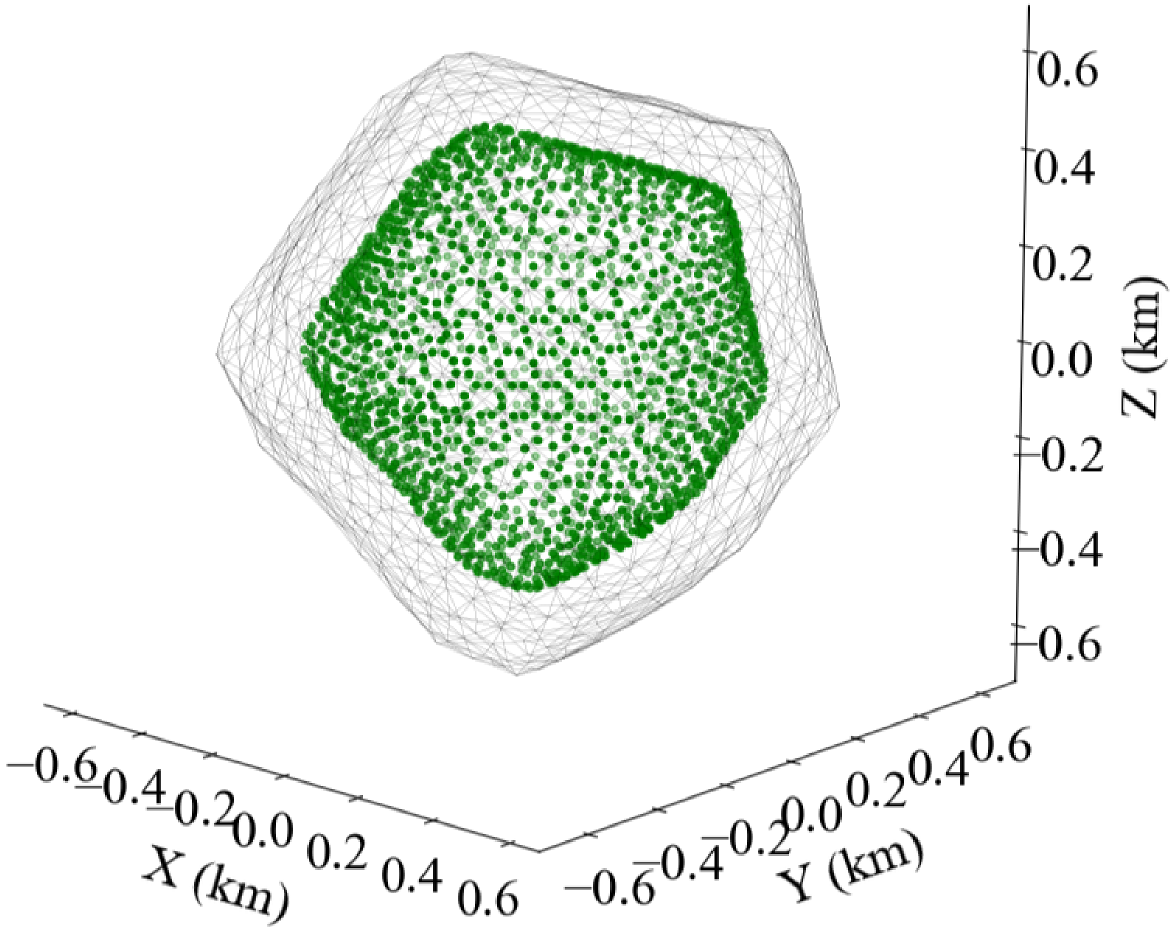

FIGURE 3.11: MASCON model of (29075) 1950DA.

more clearly in Figure 3.14 with a single trajectory generating multiple periodic points within the islands of stability between $y = -4.0\ km$ and $y = -10.0\ km$. The chaotic region remains on the exterior as the scattered dots before enclosing the section around $y \approx -16\ km$. While the energy of $H = 3 \times 10^{-7}\ \frac{km^2}{s^2}$ shows a more chaotic region, with less bounded motion as the chaotic region begins at a closer distance of $y \approx -5.0\ km$.

The resonant orbits within Figure 3.15 are of particular interest as they show a unique structure that also appears in the higher energy section in Figure 3.14, yet are more prominent within the Poincaré map of $H = 3 \times 10^{-7}\ \frac{km^2}{s^2}$. The higher energy is of great interest as it shows a more complex structure with additional islands of stability. The high energy is also easier to achieve for a spacecraft as it requires less Δv to enter into orbit around the asteroid, especially if the velocity for the transit to the asteroid is high to reduce travel time. It also is shown in the Poincaré map in Figure 3.13 that the islands of stability appear at a greater distance from the asteroid for the high energy case. For a closer look at the possibilities of resonant orbits, we will focus on the lower energy

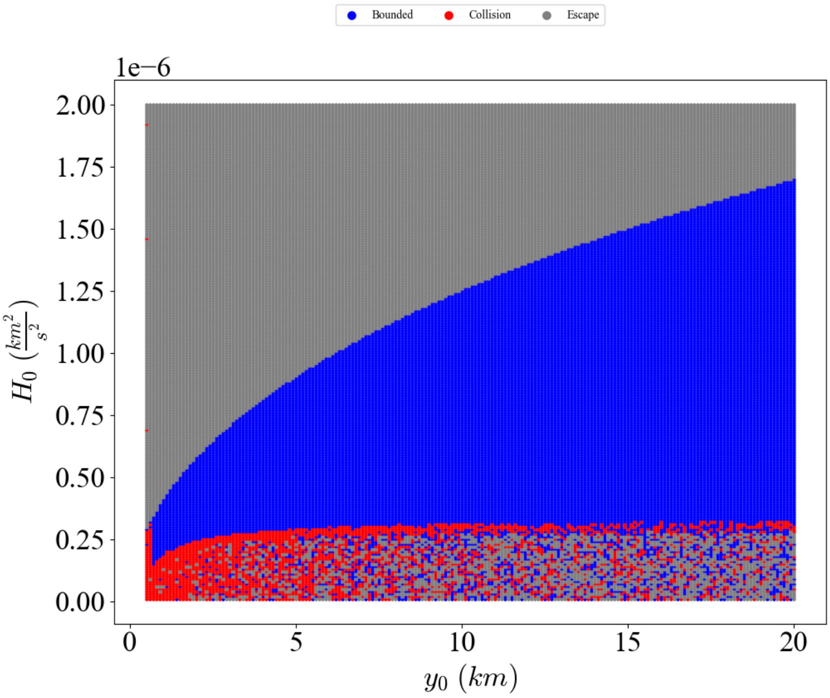

FIGURE 3.12: Survival map for 1950DA with a 60 day stability criteria.

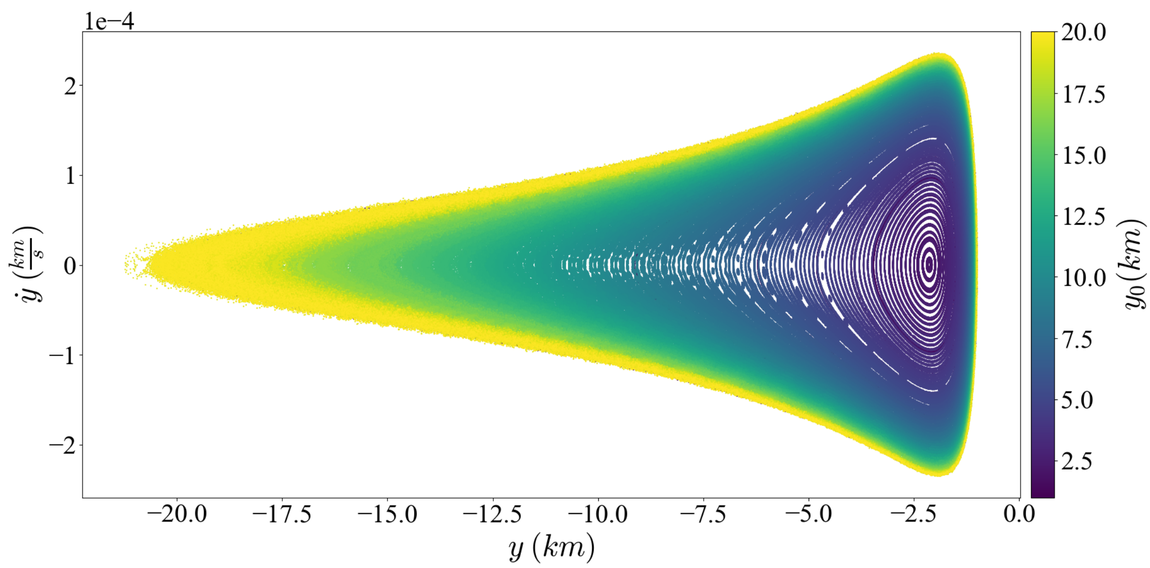

FIGURE 3.13: Poincaré Surface of Section around 1950DA for the energy $H = 4 \times 10^{-7}\ \frac{km^2}{s^2}$.

as they are more defined closer to the asteroid. The orbits that define the islands of stability that enclose the resonant orbits are shown in Figure 3.16 with initial conditions of 0.7 km and 3.0 km. This defines the separatrix in the limit of chaos and quasi-periodic motion, with resonant periodic motion in the center. The trajectories shown in Figs. 3.17 and 3.18 respectively and are matched by color to the Poincaré map.

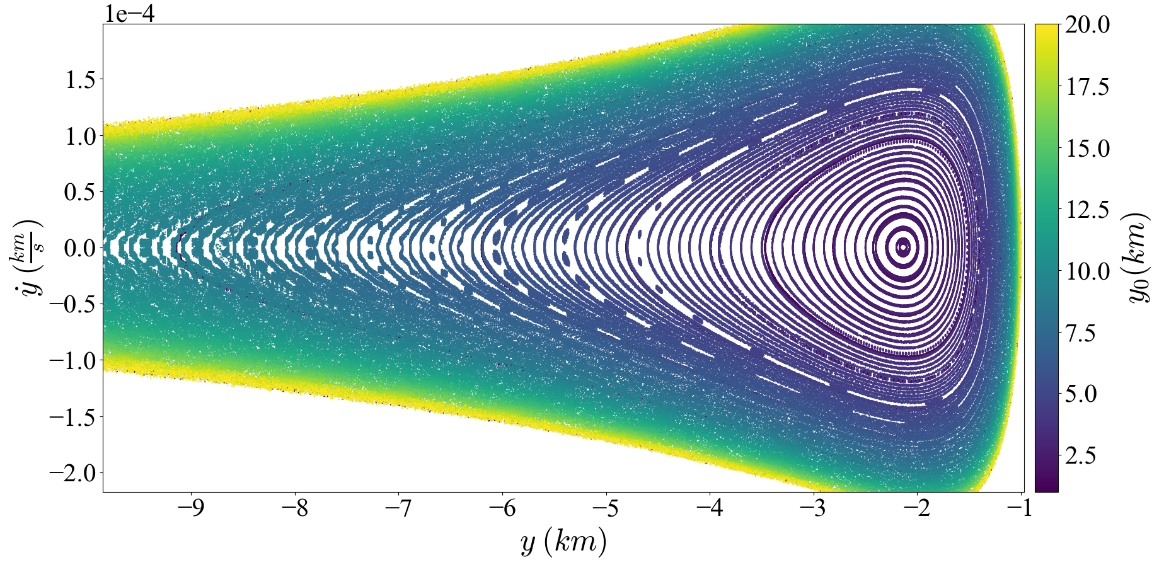

FIGURE 3.14: Interior structure of the Poincaré Surface of Section around 1950DA at the energy $H = 4 \times 10^{-7}\ \frac{km^2}{s^2}$.

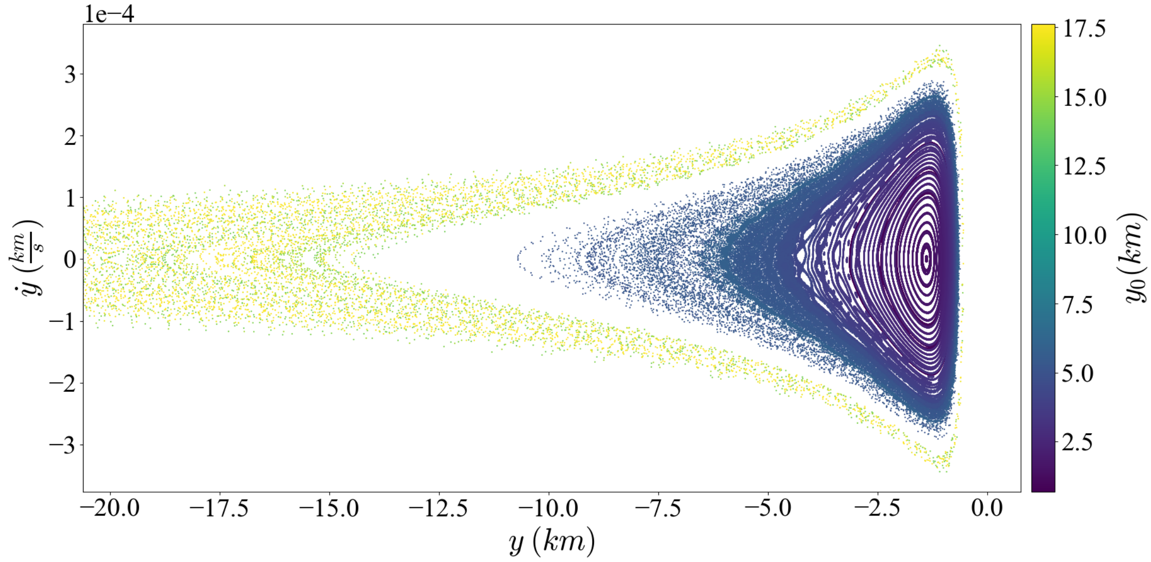

FIGURE 3.15: Poincaré Surface of Section around 1950DA at the energy $H = 3 \times 10^{-7}\ \frac{km^2}{s^2}$.

To determine if a periodic orbit is a resonant orbit we examine the spin period of the asteroid and the period of orbit. Equation 3.2 shows the approximate period of orbit with semi-major axis a and gravitational parameter of the asteroid μ Bate, 2020. With this equation the semi-major axis of the periodic orbit is used to calculate the period of orbit, and then compared to the spin period of the asteroid to determine if it is a resonant orbit, and what resonance it is in.

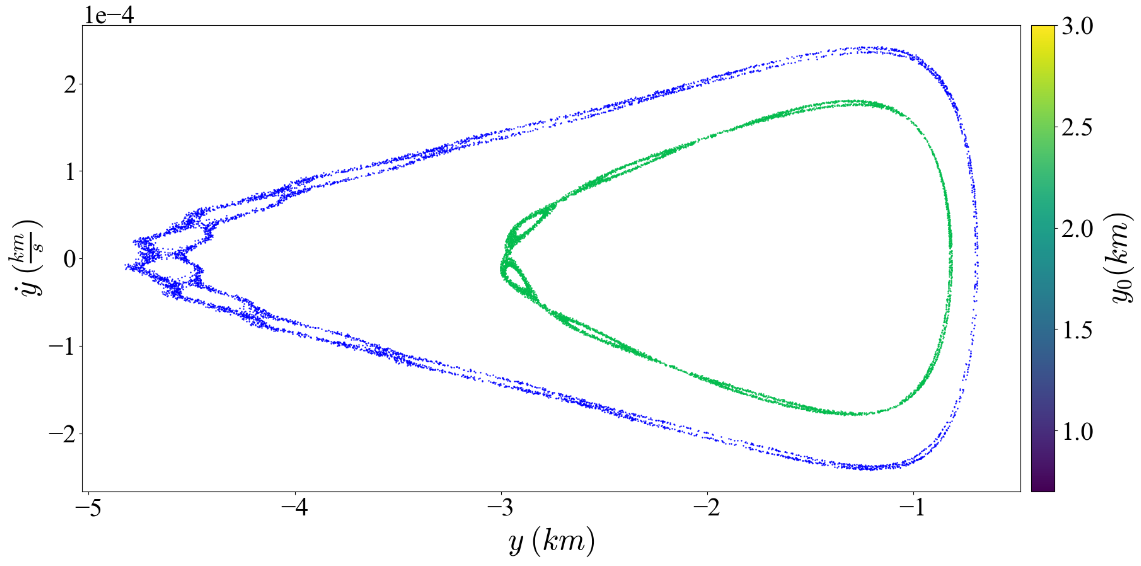

FIGURE 3.16: Poincaré Surface of Section around 1950DA at the energy $H = 3 \times 10^{-7}\ \frac{km^2}{s^2}$. The orbit in blue has the initial position at 0.7 km, green is 3.0 km.

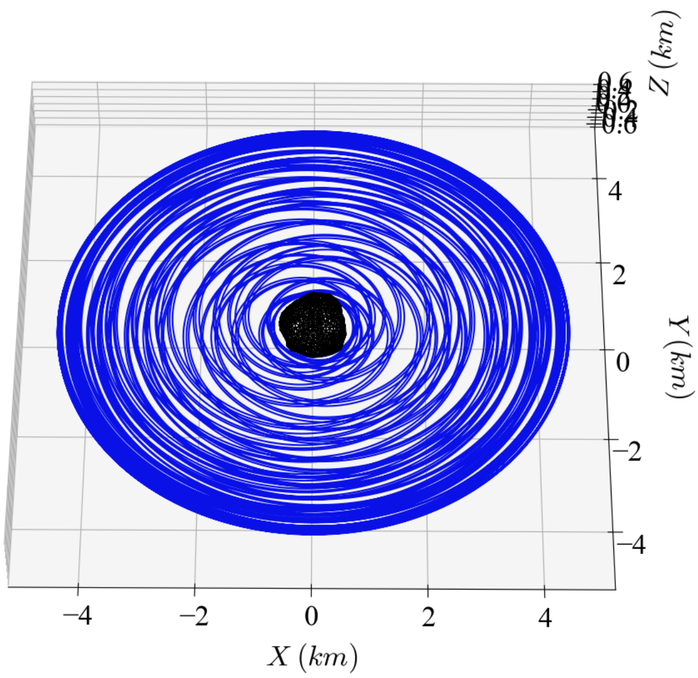

FIGURE 3.17: Orbital trajectory for the orbit 0.7 km with energy $H = 3 \times 10^{-7}\ \frac{km^2}{s^2}$.

$$T = 2\pi \frac{a^{3/2}}{\sqrt{\mu}} \tag{3.2}$$

The initial condition of 1.3812 km was chosen as it is near the center of this island, and

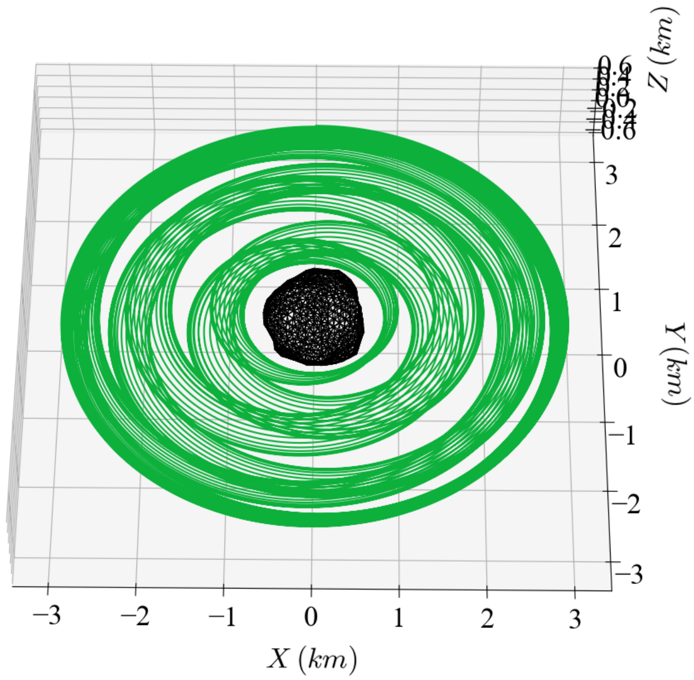

FIGURE 3.18: Orbital trajectory for the orbit 3.0 km with energy $H = 3 \times 10^{-7} \frac{km^2}{s^2}$.

the trajectory is shown in Figure 3.19. This orbit is not perfectly periodic, yet it is near periodic as it comes extremely close to returning to its initial condition. The period of this orbit was calculated to be $T \approx 7.925$ $hrs.$, and comparing this to the spin period of the asteroid of $\omega \approx 2.1216$ $hrs.$, we find that this orbit is near a 1 : 4 resonance with the asteroid's spin. This resonance is not perfect as it is a ratio of approximately 1 : 3.74, yet it is very close to the 1 : 4 resonance. This shows that a more precise selection of initial conditions can lead to a perfect resonant orbit. This orbit is also suitable for a spacecraft orbit since it requires low delta-v expenditure to keep its shape and an excellent option for asteroid mapping.

Overall, the Poincaré surface of sections shown in Figure 3.15 and Figure 3.13 show a rich structure of bounded motion regions, chaotic regions, and resonance orbits. These structures can be further analyzed to find the exact 1 : 4 resonant orbit, and the stability of these orbits can be analyzed to find potential orbits for spacecraft to utilize around 1950DA.

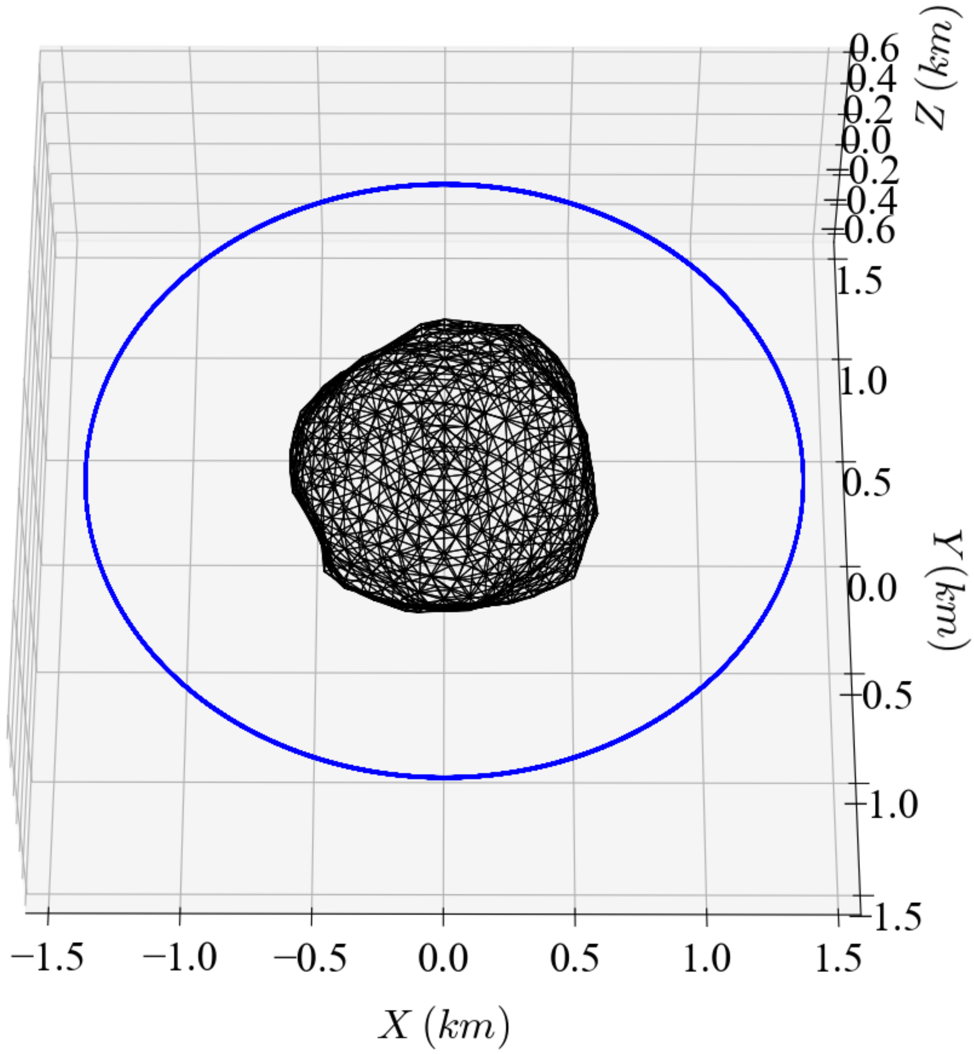

FIGURE 3.19: Orbital trajectory for the near periodic orbit at 1.3812 km with energy $H = 3 \times 10^{-7}\ \frac{km^2}{s^2}$.

Chapter 4

Preliminary Mission Planning for Asteroid 1950DA

4.1 Equilibrium Points for an Orbiting Particle

A two-dimensional Newton-Raphson method was used to find the equilibrium points in the XY-frame following the algorithm depicted by Scheeres (2012). First, we define an incremental change δx_i to the initial guess x_i. If this approximately satisfies $H_x(x_i + \delta x_i) = 0$, then we can use a Taylor series in the first order shown in Equation (4.1) to expand the function and solve for this incremental change (Scheeres, 2012). This yields the update equation shown in Equation (4.2), where we define the update as δx_i. Equation 4.3 shows the full algorithm for the Newton-Raphson method where we iteratively update our guess for the equilibrium point for i iterations.

$$H_x(x_i) + H_{xx}(x_i) \cdot \delta x_i + \cdots = 0 \tag{4.1}$$

$$\delta x_i = -H_{xx}(x_i)^{-1} \cdot H_x(x_i) \tag{4.2}$$

$$x_{i+1} = x_i + \delta x_i \tag{4.3}$$

Within Equation 4.2 we see the terms H_x and H_{xx}, which are defined as the Jacobian and Hessian of the gravitational potential. To define the Jacobian term H_x we first start with the derivative of the hamiltonian energy, Equation (2.19), where we set $\dot{x} = \dot{y} = 0$, yielding Equation 4.4 and 4.5. Here for notion we set the cartesian coordinates as (ξ, η, ζ) to differentiate from the iterative solution notation.

$$0 = \omega^2 x + U_\xi \tag{4.4}$$

$$0 = \omega^2 y + U_\eta \tag{4.5}$$

In Equation 4.4 and 4.5, we see the gradient of the asteroid's potential as Equation (2.8)and (2.9) where we defined the terms as U_ξ and U_η respectively. Along with the gradient of the potential we also see the derivatives of the Coriolis force. Equations (4.4) and (4.5) are set into the algorithm's form shown in Equation 4.6 for the XY-plane.

$$H_x = \begin{bmatrix} \omega^2 x + U_\xi \\ \omega^2 y + U_\eta \end{bmatrix} \tag{4.6}$$

Similarly using Equation (2.11) through(2.14), the Hessian is defined as H_{xx} shown in Equation 4.7 in matrix form for the XY-plane. Thus, we can define the update to the solution in Equation 4.8 for the 2D Newton-Raphson method. This is specific to the XY-plane, but can be applied to any 2D plane by changing the terms in the Hessian and Jacobian. As the Coriolis force is not present on the axis of rotation, H_x for the XZ-plane and YZ-plane only include Equation 2.10 which is the z-component of the gradient of the asteroid's gravitational potential.

$$H_{xx} = \begin{bmatrix} U_{\xi\xi} & U_{\xi\eta} \\ U_{\eta\xi} & U_{\eta\eta} \end{bmatrix} \tag{4.7}$$

$$\delta x_i = -H_{xx}^{-1} \cdot H_x = -\begin{bmatrix} U_{\xi\xi} & U_{\xi\eta} \\ U_{\eta\xi} & U_{\eta\eta} \end{bmatrix}^{-1} \cdot \begin{bmatrix} x + U_\xi \\ y + U_\eta \end{bmatrix} \tag{4.8}$$

The Newton-Raphson method in two-dimensions was then expanded to three-dimensions in Equation (4.9), where we now include the Z-component of the gravitational potential gradient and its Hessian. This allows for the finding of equilibrium points in 3D space around the asteroid given the initial condition for $i = 0$ with $x_i = [\xi_0, \eta_0, \zeta_0]^T$.

$$\delta x_i = -\begin{bmatrix} U_{\xi\xi} & U_{\xi\eta} & U_{\xi\zeta} \\ U_{\eta\xi} & U_{\eta\eta} & U_{\eta\zeta} \\ U_{\zeta\xi} & U_{\zeta\eta} & U_{\zeta\zeta} \end{bmatrix}^{-1} \cdot \begin{bmatrix} \xi + U_\xi \\ \eta + U_\eta \\ U_\zeta \end{bmatrix} \tag{4.9}$$

4.1.1 Equilibrium Points Stablity analysis

The critical theorem in determining the stability of an equilibrium point for a rotating asteroid is shown in Equation 4.10 and 4.11, and is derived from the Hessian matrix of the gravitational potential (Jiang et al., 2013). This theorem states that if and only if the four conditions in Equation 4.10 are satisfied then the equilibrium point is stable.

$$\begin{cases} U_{xx} + U_{yy} + U_{zz} + 4\omega^2 > 0 \\ U_{xx}U_{yy} + U_{yy}U_{zz} + U_{zz}U_{xx} + 4\omega^2 U_{zz} > U_{xy}^2 + U_{yz}^2 + U_{xz}^2 \\ U_{xx}U_{yy}U_{zz} + 2U_{xy}U_{yz}U_{xz} > U_{xx}U_{yz}^2 + U_{yy}U_{xz}^2 + U_{zz}U_{xy}^2 \\ A^2 + 18ABC > 4A^3C + 4B^3 + 27C^2 \end{cases} \tag{4.10}$$

$$\begin{cases} A = U_{xx} + U_{yy} + U_{zz} + 4\omega^2 \\ B = U_{xx}U_{yy} + U_{yy}U_{zz} + U_{zz}U_{xx} - U_{xy}^2 - U_{yz}^2 - U_{xz}^2 + 4\omega^2 U_{zz} \\ C = U_{xx}U_{yy}U_{zz} + 2U_{xy}U_{yz}U_{xz} - U_{xy}^2 U_{zz} - U_{yz}^2 U_{xx} - U_{xz}^2 U_{yy} \end{cases} \tag{4.11}$$

4.1.2 Equilibrium Points of 1950DA in Two and Three-Dimensions

Both the 2D and 3D Newton-Raphson methods were coded into Python and applied to 1950DA to try and find the equilibrium points of the asteroid. The main program includes two additions to the algorithm, the first is a step control to avoid the Hessian becoming singular. This is implemented by finding the norm of the incremental change δx_i, and limiting it to a step size of 1.0 km. This allows for smaller changes and keeps the solution from diverging. The second addition is the tolerance setting which breaks the iteration loop once the norm of the increment change is less than 1.0×10^{-6} km. This allows for the algorithm to converge more quickly and avoid unnecessary iterations as the change will be only a millimeter and wont have any significant impact on the solution. With this the maximum number of iterations was set to 1×10^6 where if the algorithm reaches the iteration limit the solution is flagged as did not converge and is not included within the results.

For the 2D equilibrium points, the zero-velocity curves of 1950DA were plotted in the XY-plane, YZ-plane, and XZ-plane. These zero-velocity curves gives some insight into the possibilities of equilibrium positions. Yet as shown in Figure 4.1 through Figure 4.3, the equilibrium points appear to converge on the surface likely due to the fast rotation of 1950DA making the region around the asteroid more chaotic. Some points are seen near the separatrix of the zero-velocity curves, which define them as saddle points. This means that they are in a state of unstable equilibrium, where small perturbations can lead to significant changes in their motion. Passing these through the stability theorem showed that all points found in the 2D planes were unstable.

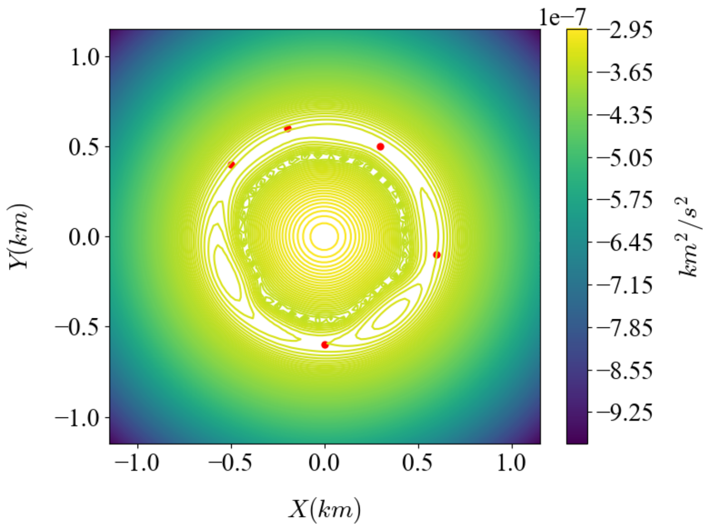

FIGURE 4.1: XY-plane slice for equilibrium points of 1950DA in 2D space.

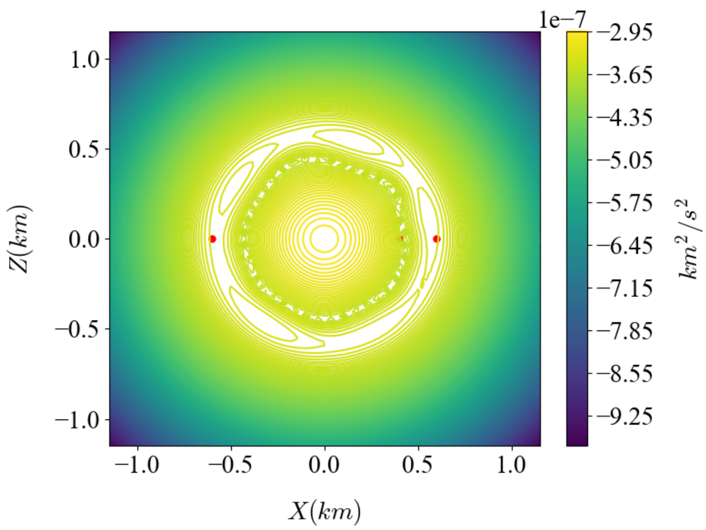

FIGURE 4.2: XZ-plane slice for equilibrium points of 1950DA in 2D space.

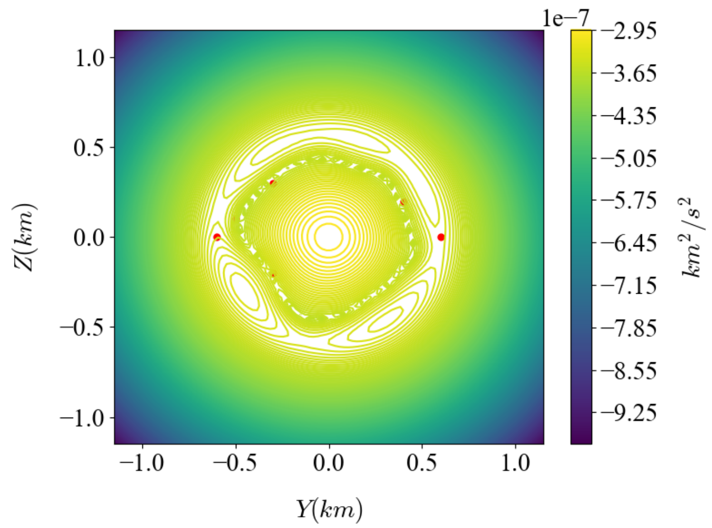

FIGURE 4.3: YZ-plane slice for equilibrium points of 1950DA in 2D space.

For the 3D equilibrium points, a grid of initial guesses was made using a mesh grid with bounds that was set as a multiple of 20 of the effective radius of the asteroid, for 1950DA this is $R_e = 0.0.575377\ km$. With this bound a mesh grid of $1,000$ points was made in the 3D space around the asteroid, covering the region of interest for the equilibrium points. Out of this a total of 166 unique equilibrium points was found, as shown in Figure 4.4, with 72 of them being stable shown in Figure 4.5. However, as can be seen in both figures, many of these points are inside the asteroid model, and thus not of interest for orbiting particles. This does serve as check for the software as there should be equilibrium points within the asteroid or near its surface. In both cases this can be seen, as the 2D equilibriums are on the surface, and the 3D equilibriums show many points within the asteroid, near the surface.

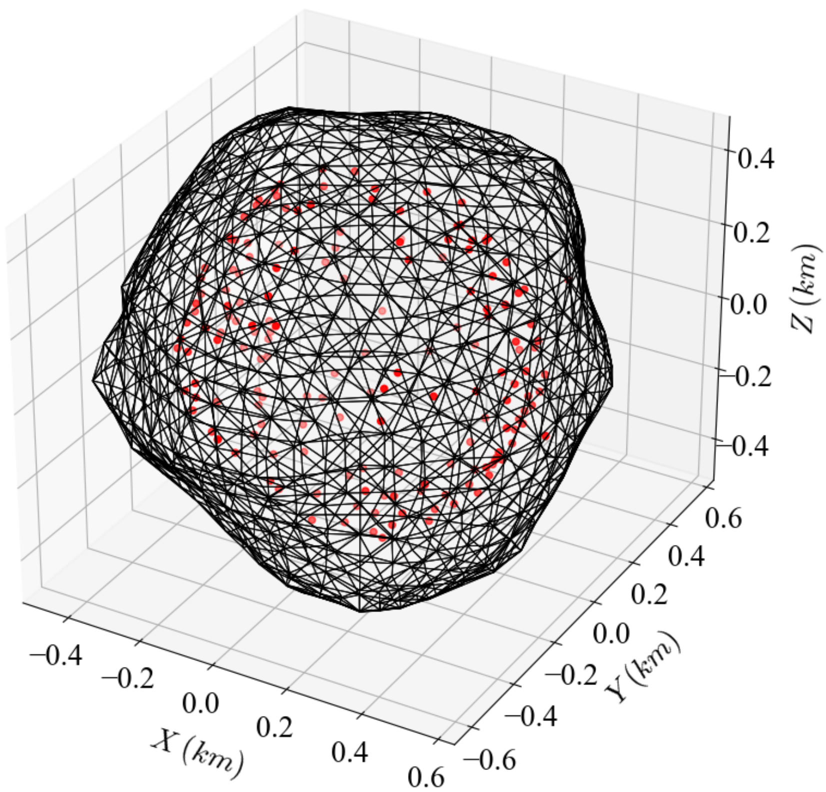

FIGURE 4.4: Equilibrium points of 1950DA in 3D space.

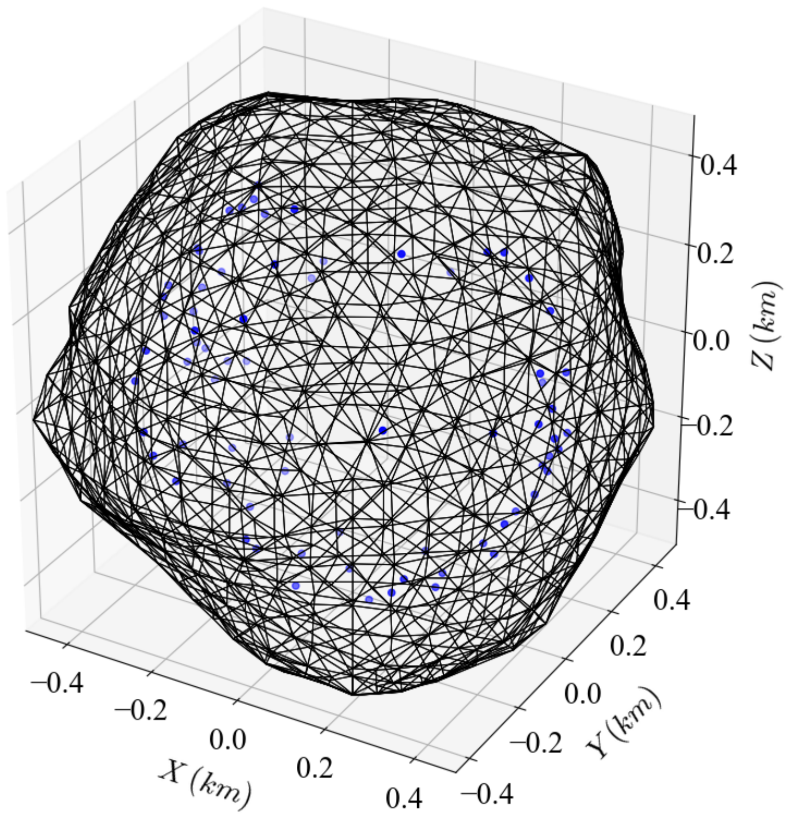

FIGURE 4.5: Stable equilibrium points of 1950DA in 3D space.

4.2 Negri-Prado Robust Path-following Control Law

Entry to the Sphere of Influence (SOI) of 1950DA from its heliocentric orbit requires maneuvering to be captured by the asteroid's gravity, especially if the mission requires a short travel time with a high velocity on transit from Earth. An example of this is the Hamiltonian energy of $H = 2.0 \times 10^{-6}\ \frac{km^2}{s^2}$ which correlates to a velocity of 7.98136 $\frac{m}{s}$ when orbiting the asteroid at a distance of $y = 10\ km$. The term ΔV refers to the change in velocity, or the difference between the initial and final velocities, required to perform a maneuver. Here we can define the selected energy as an entry velocity on arrival to 1950DA, and utilize a control law to calculate the ΔV required to be captured by the asteroid's gravity. Application of a control law to stabilize the high energy orbit could also be beneficial for efficient scanning of the asteroid before remolding and descending closer to the asteroid's surface. As previously discussed, most asteroids are scanned and re-evaluated during missions. This serves as a critical mission step, as most models derived from light curve inversion and Earth-based radar imagining yield approximate models. The only detailed models can be made from a close proximity scan of the asteroid. This feeds into making the orbit solution more refined for a desired spacecraft trajectory. Utilizing a controlled fast orbit could make detailed scans highly efficient saving propellant for other operations.

The Negri-Prado control law Negri and Prado (2020) is a robust path-following control law that stabilizes chaotic motion into Keplerian orbits; it was also applied to the spacecraft approximations for (99942) Apophis (Aljbaae et al., 2020). This path-following control utilizes a desired orbit geometry and is ideal compared to reference tracking for this problem. Instead of relying on time parameterization, this control law defines a sliding surface that uses a virtual arc-length $\vec{y}_d(\theta)$ (Negri and Prado, 2020). This is ideal for our problem as the law allows us to define a specific eccentricity and angular momentum for the spacecraft to follow, and specify the ΔV requirements for the controlled orbit.

The high energy of $H = 2.0 \times 10^{-6}\ \frac{km^2}{s^2}$ with an initial position of $y_0 = 3.0\ km$ inevitably leads to an escape trajectory from the asteroid. However, this energy is close to a region of bounded motion at $H = 0.3 \times 10^{-6}\ \frac{km^2}{s^2}$ at the same distance and serves as a viable entry velocity and position. Thus, we can apply the Negri-Prado control law for these conditions to calculate the ΔV required to be captured by the asteroid's gravity and stabilize the escape trajectory into a Keplerian orbit.

The Negri-Prado control law is designed for the MASCON system utilizing state matrix representation, allowing for the application of the control law as u. Equation (4.12) shows this in its simplest form, with the state of the system as $\dot{x}$, with state input as x

the system matrix A, the control input matrix B, and the control input vector u.

$$\dot{x} = Ax + Bu \tag{4.12}$$

The state matrix representation of this within the code takes a 7×7 form, and our x, as follows:

$$A = \begin{bmatrix} 0 & 0 & 0 & 1 & 0 & 0 & 0 \\ 0 & 0 & 0 & 0 & 1 & 0 & 0 \\ 0 & 0 & 0 & 0 & 0 & 1 & 0 \\ \omega^2 & 0 & 0 & 0 & \omega & 0 & U_\xi \\ 0 & \omega^2 & 0 & -\omega & 0 & 0 & U_\eta \\ 0 & 0 & 0 & 0 & 0 & 0 & U_\zeta \\ 0 & 0 & 0 & 0 & 0 & 0 & 0 \end{bmatrix} \qquad x = \begin{bmatrix} x \\ y \\ z \\ \dot{x} \\ \dot{y} \\ \dot{z} \\ 1 \end{bmatrix}.$$

It can be seen that the matrix $A \in \mathbb{R}^{7\times7}$ has a null state at the bottom to keep the matrix square while we include the gravitational force from the MASCONs into the system. From this, we can then use the following form to apply the control law discussed in the following section, and allow for integration in Python's `solve_ivp()` integrator. Equation (4.13) shows the full state matrix representation. Here we see the terms U_R, U_T, and U_N representing the acceleration corrections designed by the control law used for orbital tracking.

$$\underbrace{\begin{bmatrix} \dot{x} \\ \dot{y} \\ \dot{z} \\ \ddot{x} \\ \ddot{y} \\ \ddot{z} \\ 0_{\textit{null-state}} \end{bmatrix}}_{\dot{x}} = \underbrace{\begin{bmatrix} 0 & 0 & 0 & 1 & 0 & 0 & 0 \\ 0 & 0 & 0 & 0 & 1 & 0 & 0 \\ 0 & 0 & 0 & 0 & 0 & 1 & 0 \\ \omega^2 & 0 & 0 & 0 & \omega & 0 & U_x \\ 0 & \omega^2 & 0 & -\omega & 0 & 0 & U_y \\ 0 & 0 & 0 & 0 & 0 & 0 & U_z \\ 0 & 0 & 0 & 0 & 0 & 0 & 0 \end{bmatrix}}_{A} \cdot \underbrace{\begin{bmatrix} x \\ y \\ z \\ \dot{x} \\ \dot{y} \\ \dot{z} \\ 1 \end{bmatrix}}_{x} + \underbrace{\begin{bmatrix} 0 & 0 & 0 \\ 0 & 0 & 0 \\ 0 & 0 & 0 \\ 1 & 0 & 0 \\ 0 & 1 & 0 \\ 0 & 0 & 1 \\ 0 & 0 & 0 \end{bmatrix}}_{B} \cdot \underbrace{\begin{bmatrix} u_1 \\ u_2 \\ u_3 \end{bmatrix}}_{u} \tag{4.13}$$

4.2.1 Designing Control Law in Python

As discussed previously the path-following algorithm is not parameterized by time, but rather by the virtual arc length that defines the target Keplerian orbit making it ideal for controlling chaotic motion. In summary, this control law relies solely on the definition of the desired eccentricity and angular momentum vectors defined in the Two-Body problem (Negri and Prado, 2020). This creates a sliding mode control (SMC) law for our non-linear dynamical system applicable to a wide range of orbital station-keeping missions; examples presented by the authors of the control law include the OSIRIS-REx (Negri and Prado, 2020; Batista Negri and Prado, 2022). The control law defines acceleration corrections in the radial-transverse-normal (RTN) frame $\vec{u}_{RTN}$ for any Keplerian orbit, thus we can apply it to our system. This is due to the RTN frame definition, which as defined in the body fixed $(\hat{i}, \hat{j}, \hat{k})$ coordinates of an orbiting target (Curtis, 2020). To begin the definition of the controller we start with the eccentricity vector defined in Equation (4.14) with the desired orbital angles: Ω_d Longitude of the Ascending Node, ω_d Argument of the Perigee, and i_d inclination.

$$\vec{e}_d = e_d \cdot \begin{bmatrix} \cos\Omega_d \cos\omega_d - \sin\Omega_d \sin\omega_d \cos i_d \\ \sin\Omega_d \cos\omega_d - \cos\Omega_d \sin\omega_d \cos i_d \\ \sin\omega_d \sin i_d \end{bmatrix} \tag{4.14}$$

In Equation (4.14) we see the desired eccentricity vector $\vec{e}_d$ defined, along with the e_d term to help control the desired eccentricity, especially when all angles are set to zero. As can be seen if this is the case then $\vec{e}_d$ will become 1, which defines a parabolic orbit on the verge of becoming a hyperbolic escape trajectory. This form is presented in equation 12 of Batista Negri and Prado (2022) and is essential for selecting the desired eccentricity. Next, we define the desired angular momentum vector $\hat{h}_d$ as:

$$\hat{h}_d = \begin{bmatrix} \sin i_d \sin\Omega_d \\ -\sin i_d \cos\Omega_d \\ \cos i_d \end{bmatrix}.$$

Utilizing the desired eccentricity and angular momentum vectors the sliding surface $\vec{S}$ is defined as follows:

$$\vec{S} = \begin{bmatrix} (\vec{e} - \vec{e}_d) \cdot (\lambda_R \hat{r} + \hat{\theta}) \\ h - h_d \\ \hat{h}_d \cdot (\lambda_N \hat{r} + \hat{\theta}) \end{bmatrix}.$$

Here we also introduce the control terms λ_R and λ_N as design parameters which help define the convergence to the sliding surface (Batista Negri and Prado, 2022). It can be seen that the difference between the current eccentricity vector $\vec{e}$ with the desired eccentricity vector $\vec{e}_d$ defines the sliding surface. The same is true for the magnitudes of the current and desired angular momentum vector, $\vec{h}$ and $\vec{h}_d$ respectively. As will be discussed later this means $\vec{S}$ must be included in the definition for the equations of motion. Next we define the matrices F and G, used to calculate the acceleration corrections:

$$F = \frac{1}{h\mu}\begin{bmatrix} -h^2 & (2\lambda_R h - (\dot{\vec{r}} \cdot \hat{r})r)h & -\mu r \vec{e}_d \cdot \hat{h} \\ 0 & \mu r h & 0 \\ 0 & 0 & \mu r \hat{h}_d \cdot \hat{h} \end{bmatrix}$$

$$G = \frac{h}{r^2}\begin{bmatrix} (\vec{e} - \vec{e}_d) \cdot (\lambda_R \hat{\theta} - \hat{r}) \\ 0 \\ \hat{h}_d \cdot (\lambda_N \hat{\theta} - \hat{r}) \end{bmatrix}$$

These matrices carry two main assumptions, the first being that the magnitudes of the position vector $\vec{r}$ and angular momentum vector $\vec{h}$ are not zero. The second is that far a given angle β, defined as $\cos\beta = \hat{h} \cdot \hat{h}_d$, must be bound as under $\frac{\pi}{2}$ or $\beta < 90°$. If these assumptions remain true then the matrix F is always invertible. The event that these assumptions would be invalid is rare in station keeping as this would either be a non-moving target, or too chaotic of a trajectory respectively. An algorithm is presented to circumvent these matrices if needed for $\beta \geq 90°$ (Batista Negri and Prado, 2022). The saturation function, used in the controller, is defined as follows:

$$sat(\alpha, \beta) = \begin{cases} +1 & \alpha > \beta \\ \frac{\alpha}{\beta} & -\beta \leq \alpha \leq \beta \\ -1 & \alpha < -\beta \end{cases}.$$

The saturation function itself helps to saturate the controller with values of 1 or -1 depending on the given parameters. It is used in SMC to avoid discontinuous control inputs, yielding a convergences boundary for the sliding surface at some performance costs (Batista Negri and Prado, 2022). Here we define the gain matrix K and the Φ design matrix utilized by the saturation function to control the input for the sliding surface $\vec{s}$:

$$\Phi = \begin{bmatrix} d_R \\ d_T \\ d_N \end{bmatrix} = n_\Phi diag(K) \qquad K = \begin{bmatrix} k_{11} & 0 & 0 \\ 0 & k_{22} & 0 \\ 0 & 0 & k_{33} \end{bmatrix}.$$

The parameter n_Φ is defined to select the size of the boundary about the sliding surface and is used for creating the control matrix Φ from the gain matrix K. The gain matrix K also carries with it inequalities that help specify its design to the system. They are presented with the terms D_R, D_T, D_N representing the disturbance matrix terms in the RTN frame. The inequalities are as follow:

$$
\begin{aligned}
k_{11} &\geq \frac{h}{\mu} D_R + \left| \frac{2\lambda_R h - (\dot{\vec{r}} \cdot \hat{r}) r}{\mu} \right| D_T + \frac{r \left| \hat{e}_d \cdot \hat{h} \right|}{h} D_N \\
k_{22} &\geq r D_T \\
k_{33} &\geq r \frac{\hat{h}_d \cdot \hat{h}}{h} D_N
\end{aligned}
$$

The disturbance matrices are the approximation of the knowns and unknowns of the system. The disturbance due to the spin state in the body frame is an example of an unknown (Batista Negri and Prado, 2022). Using the F, G, K, Φ matrices along with the sliding surface $\vec{s}$ and the saturation function, we now define the equation for the acceleration corrections as:

$$
\vec{u}_{RTN} = -F^{-1}(G + Ksat(\vec{s}, \Phi)) = \begin{bmatrix} U_R \\ U_T \\ U_N \end{bmatrix} \tag{4.15}
$$

We then use the following relation to rotate the corrections into our reference frame:

$$
\vec{u} = U_R \hat{r} + U_T \hat{\theta} + U_N \hat{h} = \begin{bmatrix} u_1 \\ u_2 \\ u_3 \end{bmatrix} \tag{4.16}
$$

Where we define the unit vectors of the RTN frame as follows:

$$
\hat{r} = \frac{\vec{r}}{\|\vec{r}\|} \qquad \hat{h} = \frac{\vec{h}}{\left\|\vec{h}\right\|} \qquad \hat{\theta} = \hat{h} \times \hat{r}
$$

The position and velocity vector is defined within the state vector x:

$$
\vec{r} = \begin{bmatrix} x & y & z \end{bmatrix}^T \qquad \dot{\vec{r}} = \begin{bmatrix} \dot{x} & \dot{y} & \dot{z} \end{bmatrix}^T
$$

which are used to calculate the eccentricity and angular momentum vectors as follows:

$$\vec{e} = \frac{1}{\mu}(\dot{\vec{r}} \times \vec{h} - \mu\hat{r}) \qquad\qquad \vec{h} = \vec{r} \times \dot{\vec{r}}$$

Equation (4.16) is used as our systems control input u for the integration of the system $\dot{x} = Ax + Bu$. Yet one key part of the design of this control law is to define specific parts of the controller inside the equations of motion being integrated. This is because for each integration step new eccentricity and momentum vectors $(\vec{e}, \vec{h})$ will need to be calculated to define the error between the current and desired eccentricity and angular momentum vectors.

The sliding surface $\vec{S}$ along with the F and G matrices are all defined within the equations to be integrated and are solved for with each step. This is because they contain various terms for the difference between the desired and current eccentricity and angular momentum vectors. These are then used to calculate the acceleration corrections $\vec{u}_{RTN}$. As can be seen in the source code, The gain matrix K along with Φ, and the disturbance matrix D, all need to be designed for the system initially, thus they are outside of the equation of motion definition.

For the design of the disturbance matrix D, we can hold the assumption that $D = D_R = D_T = D_N$. In practice, the disturbance matrix can be chosen, relative to the units and order of magnitude as the total gravitational acceleration in the body fixed rotating frame. In this regard, we base our choice on the disturbances at our initial position when calculating the velocity as shown in Table 4.1.

TABLE 4.1: Disturbance Matrix Approximation

H	$2.0 \times 10^{-6} \frac{km^2}{s^2}$
U_{Pseudo}	$4.269628 \times 10^{-8} \frac{km^2}{s^2}$
Centrifugal Force	$3.092329 \times 10^{-6} \frac{km^2}{s^2}$

Using the initial conditions of $H = 2.0 \times 10^{-6} \frac{km^2}{s^2}$ and $y_0 = 3.0\ km$, the rough estimation of the centrifugal force can be made, which aids in designing of the D and subsequent matrices. This along with the pseudo-potential shows our disturbances are in the order of $\approx 1 \times 10^{-6} \frac{km^2}{s^2}$. Thus our selection of $\approx 1 \times 10^{-14}$, shows we want our ΔV corrections to be in the order of m^2 while remaining in km units and within the same order of magnitude as the known forces.

TABLE 4.2: Gain matrix adjustment parameters.

k_{11}	1.0×10^9
k_{22}	1.0×10^{15}
k_{33}	1.0×10^9

4.2.2 Initial Controller settings:

The disturbance matrix was set as follows:

$$D = \begin{bmatrix} 1.0 \times 10^{-14} \\ 1.0 \times 10^{-14} \\ 1.0 \times 10^{-14} \end{bmatrix}$$

which is our approximation of the disturbances given our results for the pseudo-potential and the centrifugal force. From this we can then design the gain matrix K and Φ, with adjustment parameters for the inequality shown in Table 4.2.

The gain matrix adjustment parameters in Table 4.2 ensure the controller is properly tuned for the specific dynamics of the system. This is done through testing and iterating on the control inputs to achieve the desired performance. With this, the gain matrix K and Φ are defined as follows:

$$K = \begin{bmatrix} 1.346396 \times 10^{-9} & 0 & 0 \\ 0 & 3.100 \times 10^{-14} & 0 \\ 0 & 0 & 1.006776 \times 10^{-8} \end{bmatrix} \quad \Phi = \begin{bmatrix} 6.731980 \times 10^{-11} \\ 1.5500 \times 10^{-15} \\ 5.033882 \times 10^{-11} \end{bmatrix}.$$

Parameters: $\lambda_R = \lambda_N = 0.53$, $n_\Phi = 0.05$ with all angles set to zero; $i_d = 0°$, $\Omega_d = 0°$, $\omega_d = 0°$ and the eccentricity is set $e_d = 0.005$, to define a circular orbit at an approximate zero eccentricity. This is key as the defined orbit has too low of an altitude to make a parabolic orbit without the dangers of low altitude passes causing a possible collision with the asteroid.

4.2.3 Results for Negri-Prado Control Law

Figure 4.6 and 4.7 show the results of the Negri-Prado SMC law effectively controlling the orbiting particle from the escape trajectory. This integration was over the course of 43200.0 *seconds* or 12.0 *hours* which as can be seen was sufficient time to nearly escape the asteroid's gravity if uncontrolled. Figure 4.7 shows a closer view of the trajectory being controlled, and despite minor fluctuations in the orbit, it is clear that the control law is effective in keeping the orbiting particle bound to the asteroid.

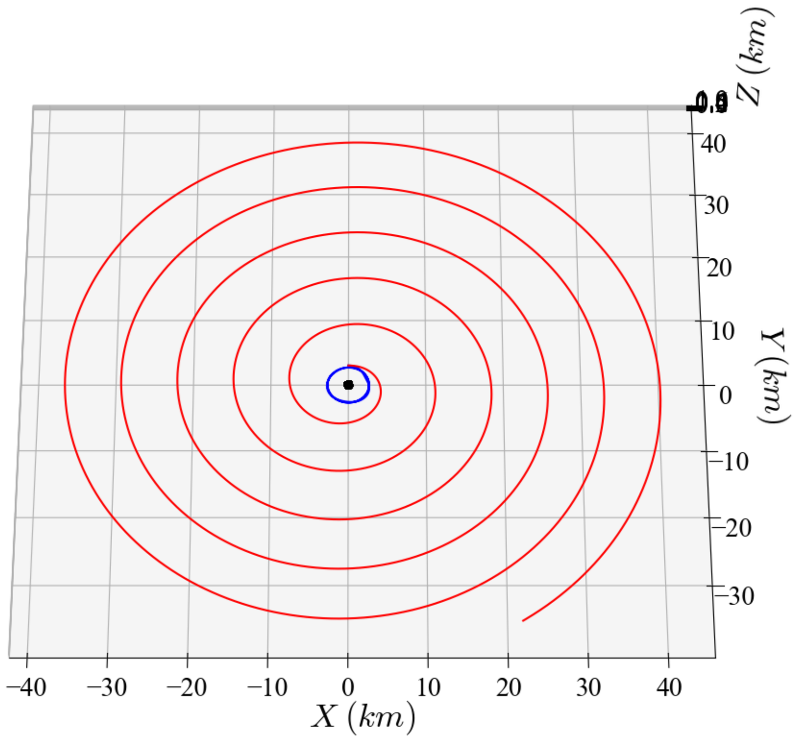

FIGURE 4.6: Expanded comparison view.

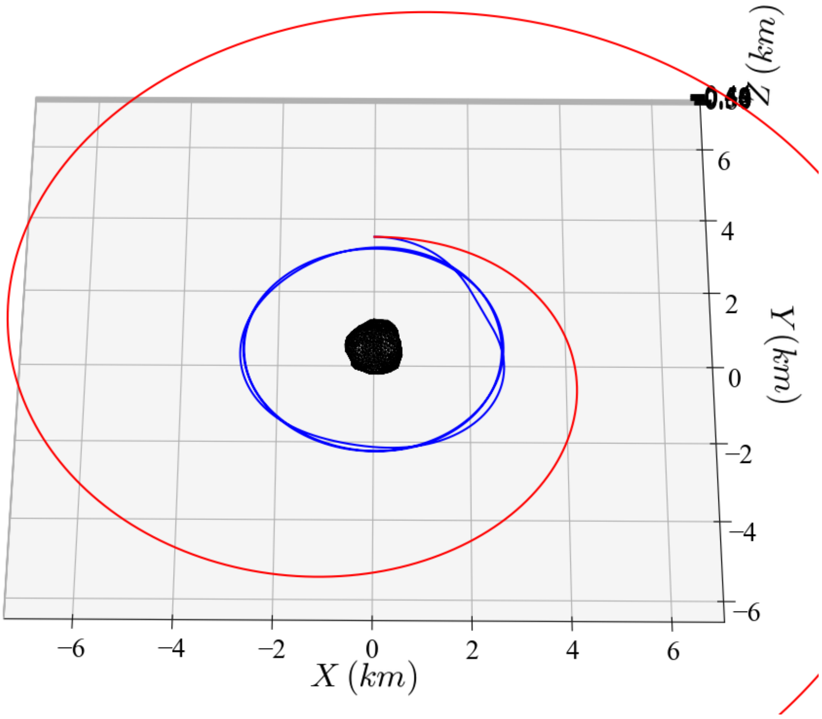

FIGURE 4.7: Comparison of controlled versus the uncontrolled escape trajectory.

The ΔV used was by the control inputs was $\approx 0.00085435\ km/s$ or $0.85435\ m/s$. Figure 4.8 shows that the controlled orbit is approaching a proper Keplerian orbit. We can see that the velocity reaches a maximum at perigee, and minimum at apogee as expected, before being plateaued by the inputs from the control inputs to stabilize the orbit. Furthermore, the Hamiltonian energy can be seen to decrease as our velocity increases and increases as it decreases storing the energy in the potential energy portion of the Hamiltonian energy.

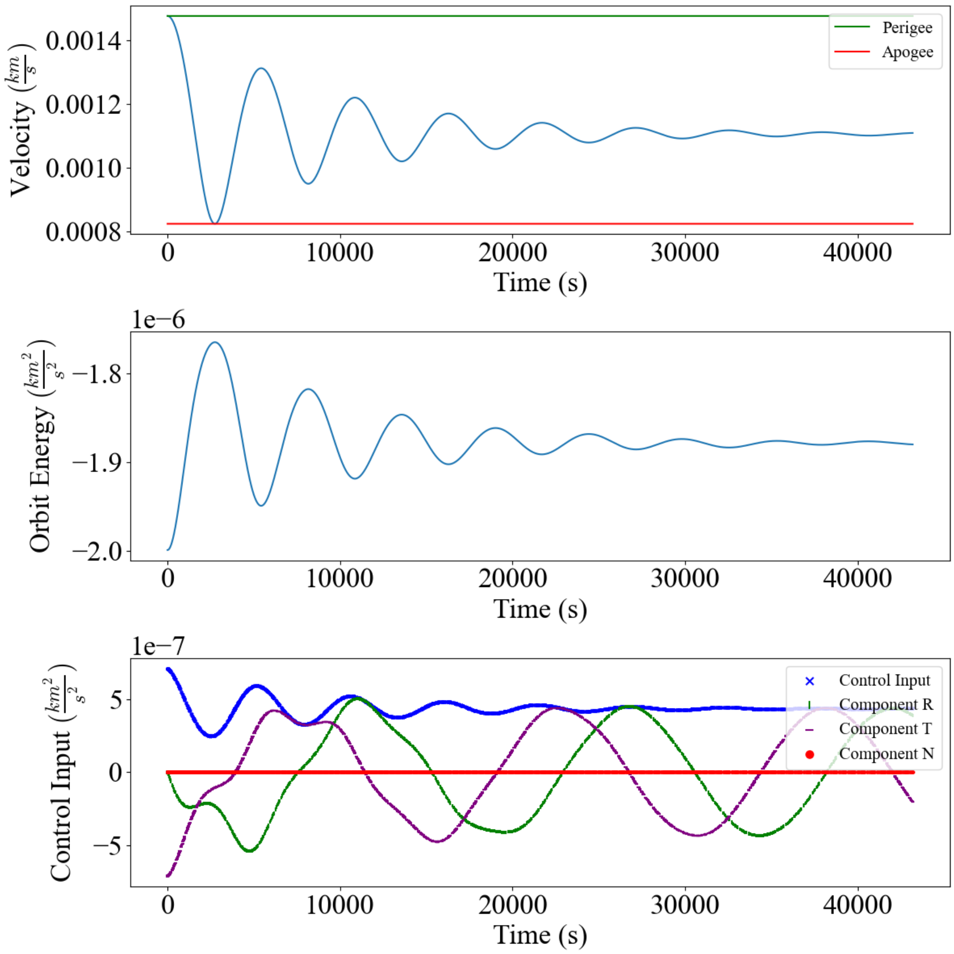

FIGURE 4.8: Velocity, Hamiltonian energy, control input, and radial error data from the comparison. The particle escaped after $\approx$ 15.985 hours ending the simulation.

The orbit shown in Figure 4.9 - 4.10 utilized a minimum ΔV of $\approx 0.00194542\ km/s$ or 1.94542 m/s for a total of 2 *days* and as can be seen the orbit's structure spans the surface of the asteroid, making it an ideal orbit for reconnaissance prior to surface landing. Examining Figure 4.11, we can see the Hamiltonian energy slowly decreasing over time, which is also reflected in the decrease in average velocity. These irregularities as compared to the center orbit are due to the control input which can be seen to reach a maximum when the velocity does. This reflects the controller trying to decrease the high energy, especially at the peak to ensure the orbit converse to the sliding surface rather than escaping. Starting from the same initial conditions as the capture trajectory,

$H = 2.0 \times 10^{-6} \frac{km^2}{s^2}$ and $y_0 = 3.0\ km$, and setting $\lambda_N = 0.0053$ allowing the orbit to develop along the normal vector for a period of 2 *days*. The orbit is controlled in a quasi-circular motion as seen in Figure 4.10 down the length of the asteroid relative to the z-axis. By analyzing the Hamiltonian energies behavior we can see that the controller ended up decreasing the energy significantly despite the high initial energy given to the orbiting particle.

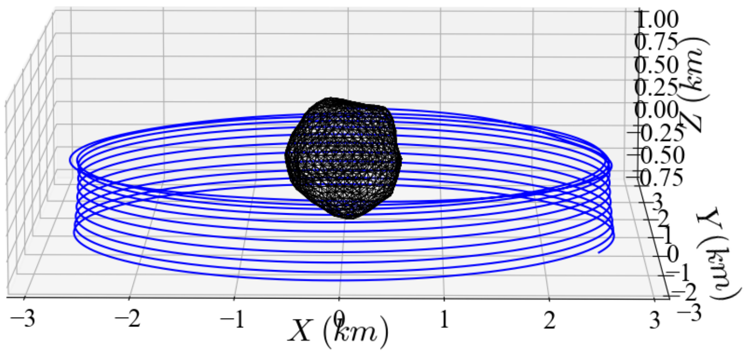

FIGURE 4.9: 2 *day* orbit, initial position $y = 3.0\ km$ and $\lambda_N = 0.0053$.

Adjusting the λ_N parameter, inherently linked to the normal component, as can be seen in the definition of the F and G matrices, λ_N takes the N position of the RTN frame. Thus, decreasing this to $\lambda_N = 0.0053$, allows the control law to not give as much weight to the normal component of the acceleration corrections. This allows the orbit to develop in the z-direction, which is ideal for scanning the asteroid's surface. This is ideal for reconnaissance prior to landing on the surface, as most asteroid missions require a detailed scan of the asteroid to refine the shape model and determine a safe landing site.

4.2.4 Fine Tuning the Negri-Prado Law

To minimize the ΔV requirements for the initial capture trajectory the term n_Φ is set to 10.0 which allows for optimal performance for the convergences to the sliding surface with minimal error (Batista Negri and Prado, 2022). While decreasing the λ_N parameter to 0.0053 allowed for a scanning orbit, increasing this parameter to $\lambda_N = 2.53$ allowed for a more stable orbit with less drift in the z-direction. This was at a cost of $\Delta V \approx 0.007336967\ km/s$ or $\Delta V \approx 7.336967\ m/s$. By increasing the parameter linked to the radial component to $\lambda_R = 2.53$ we saw a significant decrease in the amount of required ΔV to keep this orbit of only $\approx 0.006923692\ km/s$ or $\approx 6.923692\ m/s$. With this the orbit shown in Figure 4.12 was simulated for a total of 10 *days* and showed a orbital trajectory that was quasi-circular in nature and close to a periodic motion.

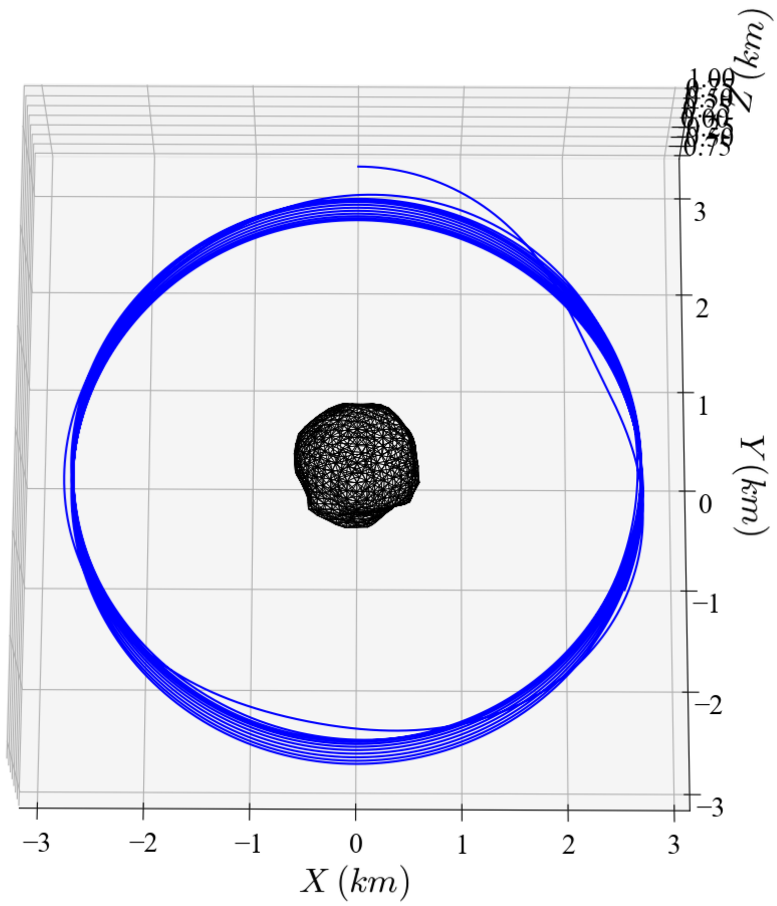

FIGURE 4.10: Top view of 2 *day* orbit

The refinement of the Negri-Prado SMC law settings can be conducted to optimize the required ΔV of either the scanning or station-keeping trajectories. This can also yield other useful orbits for further mission objectives. The key to this controller is the refinement of each chosen parameter with regards to the desired motion. By adjusting the λ_N parameter linked to the normal component of the acceleration correction matrices, and subsequently the acceleration correction $\vec{u}$, we see a control of the normal or z orbital direction. Whereas the λ_R parameter is linked to the radial component of the acceleration correction matrices. Adjusting this parameter allows for a more stable orbit with less radial error, thus creating a more periodic motion with the orbital trajectory.

The results of the simulations yielded a proper implementation of the Negri-Prado path-following SMC law for Keplerian orbits. The initial comparison showed that an uncontrolled particle will escape while the SMC shows a required $\Delta V \approx 0.85435\ m/s$ in order to stabilize the particle's motion into a quasi-periodic orbit. Allowing the simulation to develop for a period of 2 *days* with an decrease in control on the normal component λ_N yielded an orbital motion ideal for scanning the entire asteroid's surface. This could save propellant and resources, given that most spacecraft are already

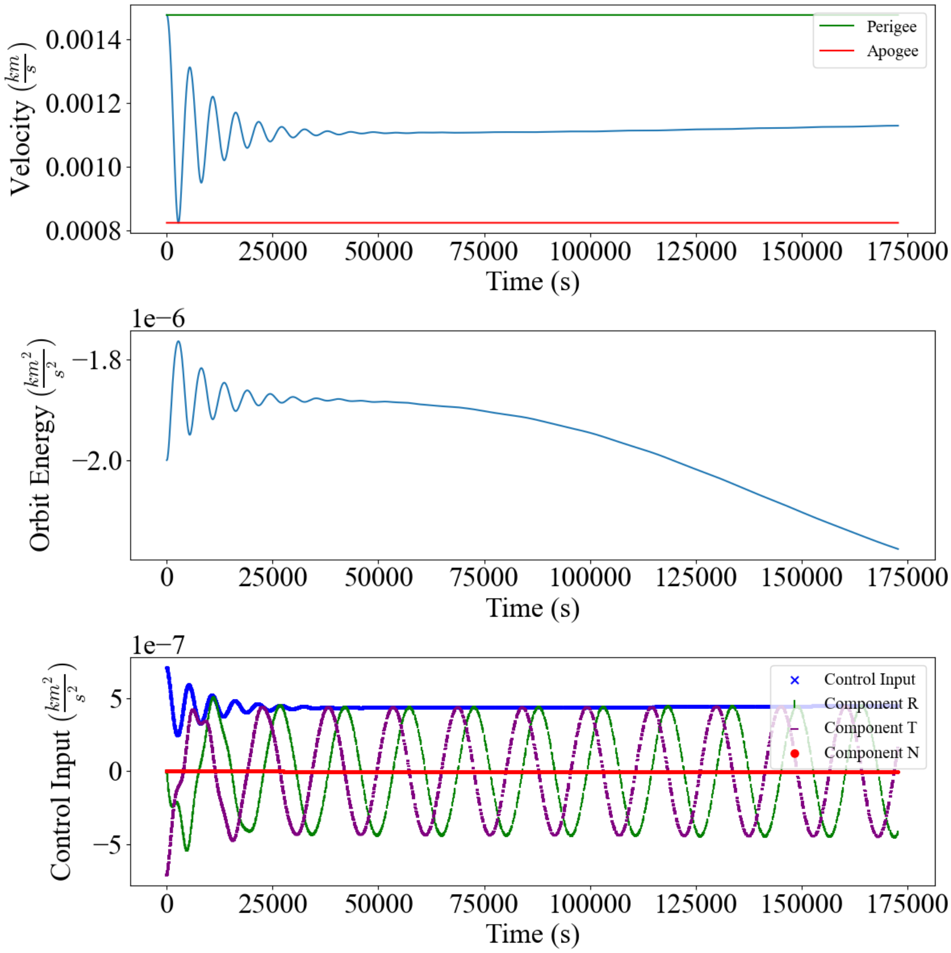

FIGURE 4.11: Velocity, Hamiltonian energy, control input, and radial error data from the 2 *day* orbit.

scrutinized for weight reduction this is vital for additional mission operations. By refining the parameters of the control law, a station-keeping trajectory was found to be quasi-periodic in nature and held for 10 *days*. This was at a cost of $\Delta V \approx 6.923692\ m/s$, and achieved by adjusting the radial and normal component parameters λ_R and λ_N respectively along with setting the convergence parameter n_Φ to an optimal value.

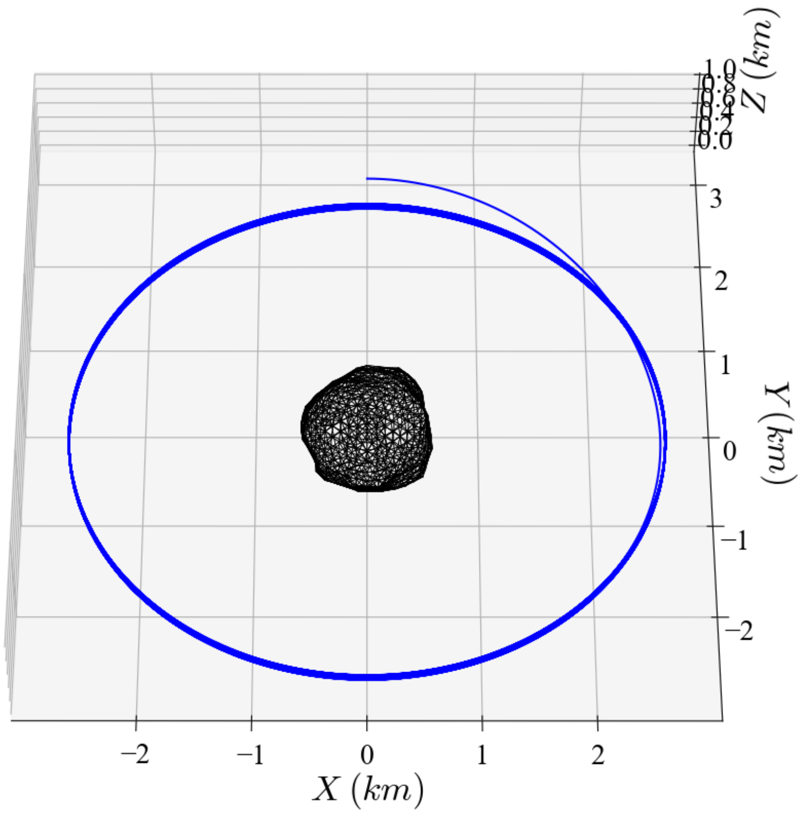

FIGURE 4.12: 10 *Day* orbit.

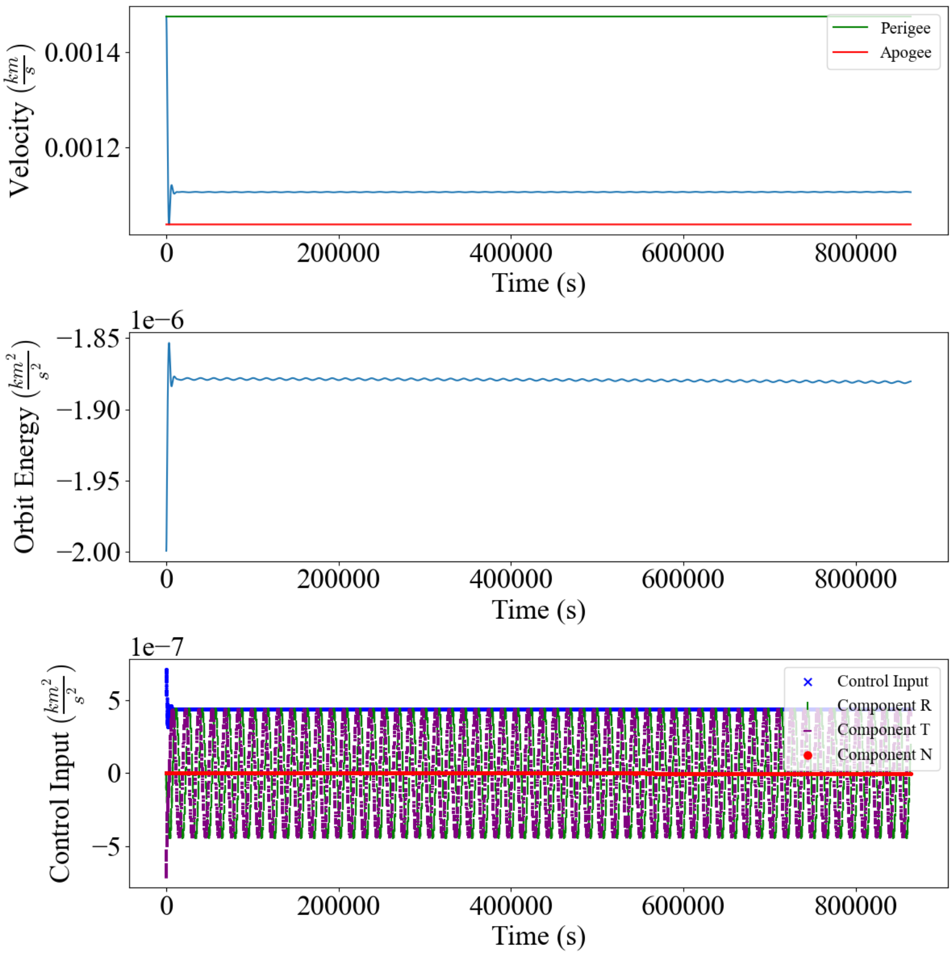

FIGURE 4.13: Velocity, Hamiltonian energy, and control input of the 10 *Day* orbit.

4.3 Landing Trajectories for Asteroid 1950DA

Utilizing the collision trajectories, we can define an efficient landing trajectory to the surface of 1950DA. This is done by defining the velocity on impact as the ΔV required to reduce the velocity to zero and land safely on the asteroid's surface rather than colliding with the surface. Table 4.3 summarizes the required ΔV for the landing including transfers to a low energy orbit of $H = 2.0 \times 10^{-8}\ \frac{km^2}{s^2}$ from the high energy orbit $H = 2.0 \times 10^{-6}\ \frac{km^2}{s^2}$ which was controlled to be a capture trajectory using the Negri-Prado control law. This gives a total $\Delta V \approx 1.455312\ m/s$ to land on the surface from the controlled capture trajectory. Figure 4.14 and 4.15 show the landing trajectory from the position of $y_0 = 3.0\ km$ down to the surface of 1950DA.

TABLE 4.3: ΔV for Landing on 1950DA

Transfer from high to low energy	$\Delta V = 0.696788\ m/s$
Landing on surface	$\Delta V = 0.758524\ m/s$
Total	$\Delta V = 1.455312\ m/s$

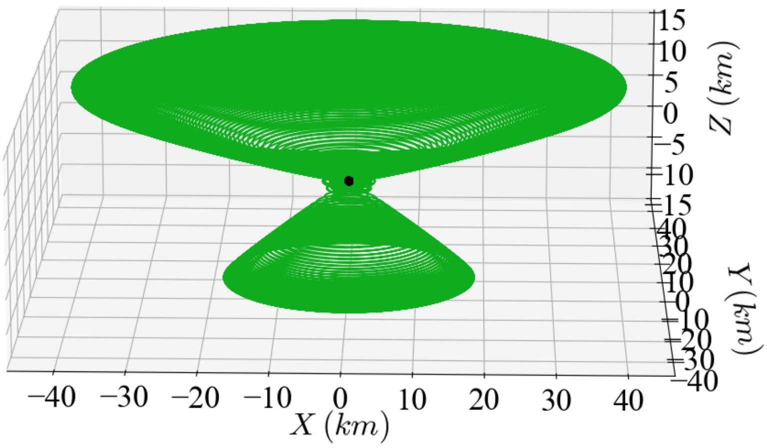

FIGURE 4.14: Landing trajectory from high energy orbit to surface of 1950DA.

It can be seen in Figure 4.14 that the landing takes some time to reach the surface, this is due to the lowered energy, and the trajectory reaches the limits of the Hill sphere before descending to the surface. Figure 4.15 shows the final portion of the landing trajectory with the landing position near the southern pole of the asteroid.

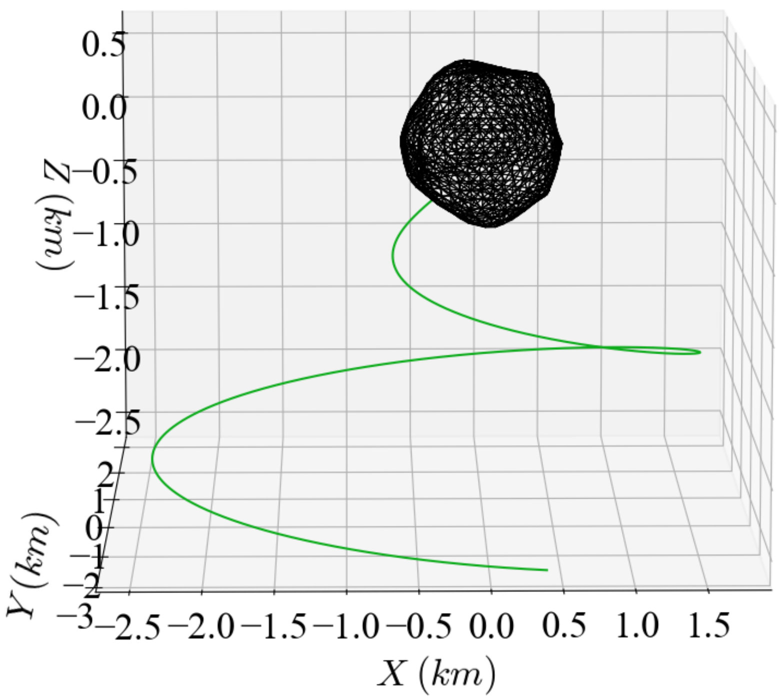

FIGURE 4.15: Final position of landing trajectory from high energy orbit to surface of 1950DA.

Chapter 5

Reduced MASCON Model Using Machine Learning

5.1 KMeans Clustering of 1950DA

In order to enhance to the computational speed of the MASCON model, a reduced model was considered. This was carried out by clustering the MASCONs of the original model into a smaller number of clusters utilizing machine learning methods. The method chosen for this work was KMeans clustering, a popular unsupervised learning algorithm used for partitioning data into distinct clusters based on their features [1]. The algorithm works by partitioning the data into k clusters, where each data point belongs to the cluster with the nearest mean. The algorithm iteratively updates the cluster centroids and reassigns data points until convergence is reached. The number of clusters k is the main hyperparameter that needs to be specified before running the algorithm (Raschka, 2022).

The KMeans algorithm was implemented using the `sklearn` library in Python, and tested on the MASCON model of 1950DA. The main control of the hyperparameter was linked to a total percent reduction, thus the user can select a desired percentage reduction and the algorithm will determine the number of clusters k, and subsequently the number of MASCONs, required to achieve this reduction. The gravitational parameter of each MASCON in the reduced model was calculated by summing the gravitational parameters of the original MASCONs within each cluster. The original MASCON model of 1950DA consists of 2036 MASCONs, and testing for a 50 % reduction, the reduced model consisted of 1018 MASCONs. The reduced model was compared to the original model by simulating the motion of a test particle at a distance of $y_0 = 0.7\ km$ which is well within the range of the error of Figure 3.3. Thus the model deviates from the point approximation and can be used to test the accuracy of the reduced model. The particle was simulated at an energy of $H = 3.0 \times 10^{-7}\ \frac{km^2}{s^2}$ for a total time of 5 $days$. The

[1] https://scikit-learn.org/stable/modules/generated/sklearn.cluster.KMeans.html

trajectories of the test particle for both the original and reduced models are shown in Figure 5.1, and the position error between the two models is shown in Figure 5.2. It can be seen in the trajectories of Figure 5.1 that the paths of the particle begin to diverge after a short period of time, indicating a loss of accuracy in the reduced model.

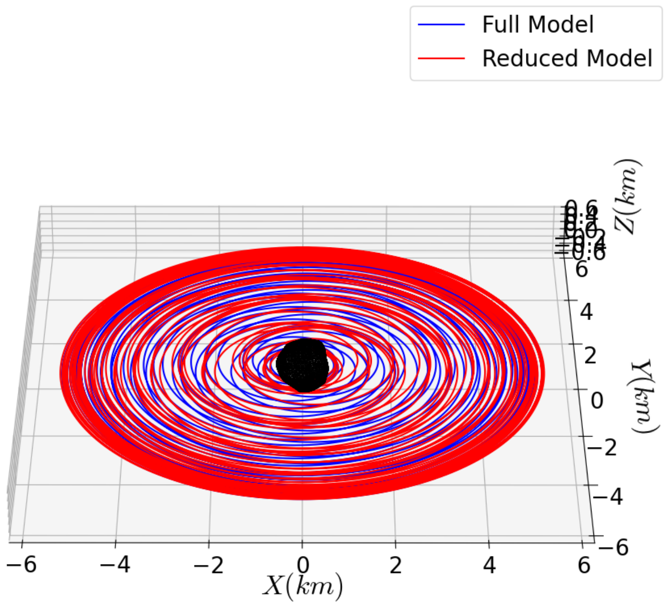

FIGURE 5.1: Trajectories for both the original and reduced MASCON models of 1950DA for a total simulation time of 5 *days*.

As seen in Figure 5.2, the position error is almost zero before a spike after almost a day, or ≈ 22 *hrs*. of simulation time. The error then returns to near zero before increasing again at the 2 and 3 day marks, with an error of 20 % after 3 *days*. At this point the error grows without returning to near zero, and this is reflected in Figure 5.1 by the varying paths the particle takes orbiting the original and reduced models. The error appears to be periodic in nature with the peaks corresponding to each day of orbit. The results show that short term accuracy is very good, with the error remaining below 1 % for almost a day, however these results are not suitable for long term simulations. The full model took 34.068 *sec*. to simulate, while the reduced model took 28.583 *sec*., thus a reduction of 16.1 % in computational time was achieved. This is a significant decrease on time, especially when considering more lengthy simulation times, yet this gain is not without error. Further testing with different percentage reductions could yield better results, yet this serves as a proof of concept for using machine learning to reduce the number of MASCONs in a model. Future work could also consider other clustering algorithms, such as HDBscan which is known for its ability to find clusters of

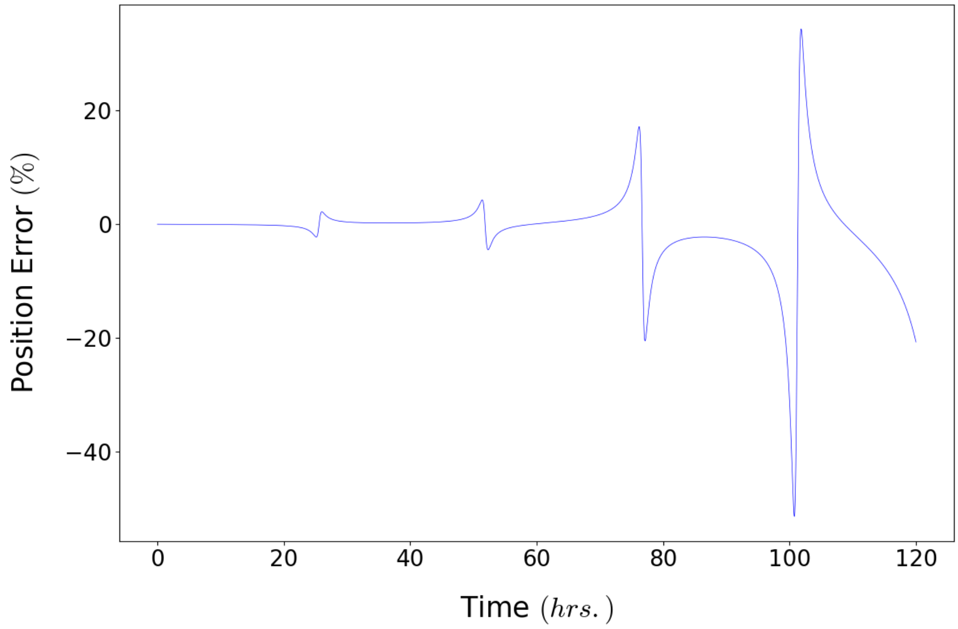

FIGURE 5.2: Position error analysis of KMeans clustering for 1950DA.

varying shapes and sizes better than KMeans [2]. Errors from integration could also be minimized by utilizing an arc integration technique, with an arc of 10 *hours* to mitigate the periodic error occurring. Additionally, Kmeans could be optimized for a smaller reduction percentage, such as 10 %, to see if the accuracy can be improved for longer term simulations. This however would not yield a significant increase in computational speed, and thus the trade off between speed and accuracy must be considered.

[2]https://scikit-learn.org/stable/modules/generated/sklearn.cluster.HDBSCAN.html

Chapter 6

Ring Dynamics of 1950DA

6.1 Simulating surface particles for 1950DA

As the rotational period of 1950DA surpass the theoretical limit of 2.2 *hrs*. for cohesion of a rubble pile like asteroid, this can be explored to determine if a ring structure is present around the asteroid. This can be done by simulating the surface particles of the asteroid and observing their behavior over time. Utilizing `trimesh` the center of each face of the 1950DA mesh was found, and a particle was placed at each of these points. Each particle was given zero initial velocity relative to the asteroid, and the simulation was run for a period of 400 days. The results of particles escaping the surface can be seen in Figure 6.1, where a ring structure is formed around the asteroid. Out of these particles that escape the surface, only seven positions were found to be stable and form a ring-like structure without escaping the asteroid's Hill sphere. Table 6.1 shows the initial positions of these particles in *km*, and define the possibilities for their long-term stability.

TABLE 6.1: Initial position of ring particles of 1950DA in *km*.

x_0	y_0	z_0
−0.0170403	−0.643269	0.0511240
−0.290456	0.535367	−0.0489060
−0.144725	−0.603597	0.0817465
−0.159064	−0.584488	0.129165
−0.173832	0.589707	−0.0496783
−0.397974	0.472538	−0.114916
−0.540931	0.302668	−0.149861

Even though the particles shown in Table 6.1 appear to form a ring structure without escaping, other forces must be considered to verify this. Thus, solar radiation pressure along with 3^{rd} body perturbations from the Sun was included in the simulation. Equations 6.1, 6.2, and 6.3 show the equations of motion used to simulate the particles considering these perturbations. As these perturbations are within the inertial frame,

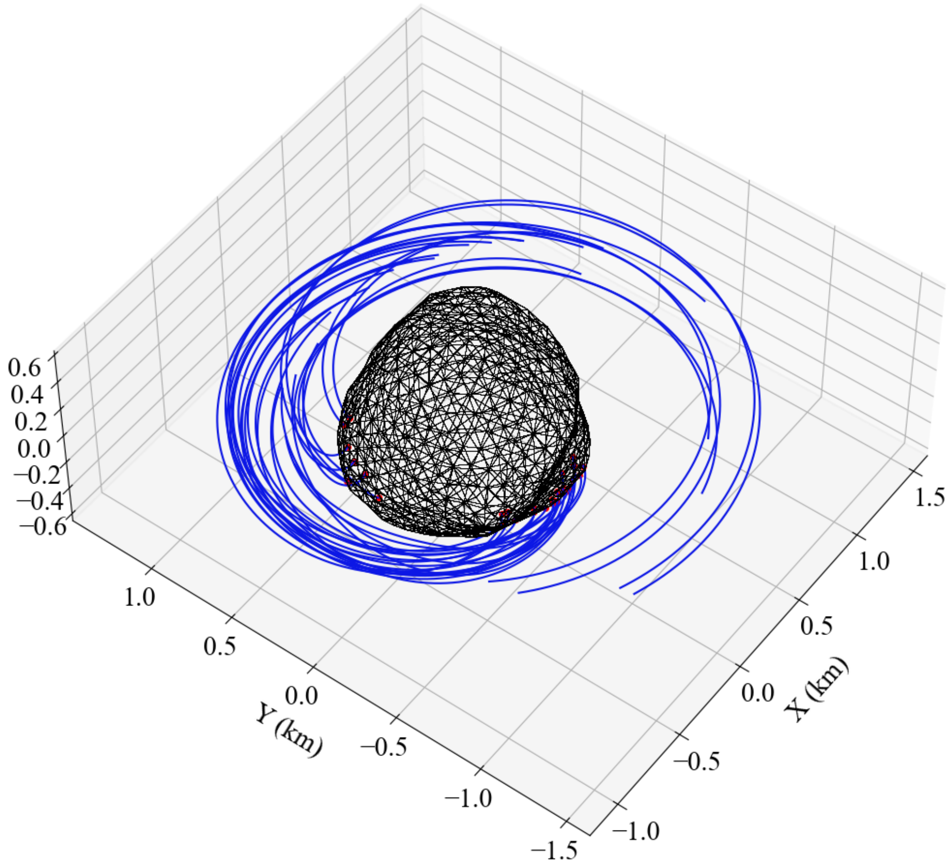

FIGURE 6.1: Surface particles of 1950DA forming a possible ring structure.

the symbol $\mathbb{R}$ is used to denote the transformation from the inertial to rotating frame (Aljbaae et al., 2020).

$$\ddot{\vec{r}} = -2\vec{\Omega} \times \dot{\vec{r}} - \vec{\Omega} \times (\vec{\Omega} \times \vec{r}) + U_r + \mathbb{R}(P_{3B}) + \mathbb{R}(P_r) \tag{6.1}$$

$$P_{3B} = \sum_{i=1, i \neq j}^{N} GM_i \left(\frac{\vec{r}_i - \vec{r}_j}{|\vec{r}_i - \vec{r}_j|^3} - \frac{\vec{r}_i}{|\vec{r}_i|^3} \right) \tag{6.2}$$

$$P_r = (1+\nu)au^2 \frac{A}{M} \frac{S}{c} \frac{\vec{r}_s - \vec{r}_\odot}{|\vec{r}_s - \vec{r}_\odot|^3} \tag{6.3}$$

Within Equation 6.3, which defines the solar radiation pressure of any orbiting particle $\vec{r}_s$ relative to the position of the sun $\vec{r}_\odot$: au is the astronomical unit, A is the cross-sectional area of the particle while M is the mass of the particle, S is the solar constant, and c is the speed of light where $S/c = 4.56316 \times 10^{-6} \frac{N}{m^2}$ (Aljbaae et al., 2020). The coefficient of reflectivity $(1+\nu)$ ranges from 1 for a completely absorbing surface to 2 for a perfectly reflecting surface (Vallado, 2022).

Solar radiation pressure is linked to the Area-to-Mass ratio, $\frac{A}{M}$, of the particle along with the materials coefficient of reflectivity. For 1950DA, we know very little about the composition and size, studies have suggested a composition of either nickel-iron or enstatite chondritic (BUSCH et al., 2007). With this uncertainty only guesses can be made as the the coefficient and Area-to-Mass ratio. For the coefficient of reflectivity values of 1.01, 1.15, and 1.30 were considered. The smallest value defines the minimum solar radiation pressure the particle could experience with most light being absorbed by the surface. The higher values define the possibilities that there is significant reflection from the composition of the asteroid, with the highest value defining the possibilities of ice formation on the surface. In Equation 6.4, the Area-to-Mass ratio is defined for a spherical particle of radius r and the density of the asteroid ρ shown in Table 3.2. Here, a minimum radius of 1 cm was considered with the maximum radius being 10 cm. Table 6.2 shows the Area-to-Mass ratios for different particle sizes within this range considering a total step size of 5 or 1.8 cm each step.

$$\frac{A}{M} = \frac{\pi r^2}{\rho V} = \frac{\pi r^2}{\rho 4/3\pi r^3} = \frac{3}{4\rho r} \tag{6.4}$$

TABLE 6.2: Area-to-Mass ratio for different particle sizes.

radius cm	$\frac{A}{M}$
1	0.0313
2.8	0.0112
4.6	0.00679
6.4	0.00488
8.2	0.00381
10	0.00313

Solar radiation pressure fluctuates, as it is dependent on the position relative to the Sun. Thus, the orbit of 1950DA around the Sun must be considered to accurately simulate the perturbations from solar radiation pressure. The orbit of 1950DA is highly eccentric at $e = 0.50784$ as shown in Table 3.2, with a semi-major axis of $a = 1.7009\ AU$. Below are period, aphelion, and perihilion calcuations conducted for 1950DA (Bate, 2020):

$$T = 2\pi\sqrt{\frac{a^3}{GM_\odot}} = 2.2\ yrs.$$

$$r_p = a(1-e) = 0.835933 AU$$

$$r_a = a(1+e) = 2.566 AU$$

.

The simulation is started at aphelion, as the solar radiation pressure will be at its minimum value, and continue for half the orbital period of 1.1 *yrs*. or 400 *days*. On the January 1st, 2025 1950DA is at a distance of 2.210 *AU*, thus this is taken as an approximate aphelion and defines the start of this simulation. Equation 6.5 shows the equation of motion for 1950DA relative to the Sun, where $\mu_\odot = G(M_\odot + M_{ast})$ defines the gravitational parameter of the system considering the mass of the asteroid M_{ast}, although this is negligible compared to the mass of the Sun $M_\odot$. As can bee seen in Equation 6.5 the motion is described by the point approximation defining this as a two-body problem (Bate, 2020). Figure 6.2 shows the trajectory of 1950DA relative to the Sun and Earth over the 400 *day* simulation period starting near aphelion, and proceeding past the perihelion. This trajectory allows for the minimum and maximum solar radiation pressure to be considered in the simulation of the surface particles escaping the surface.

$$\ddot{\vec{r}}_\odot = -\mu_\odot \frac{\vec{r_\odot}}{r_\odot^3} \tag{6.5}$$

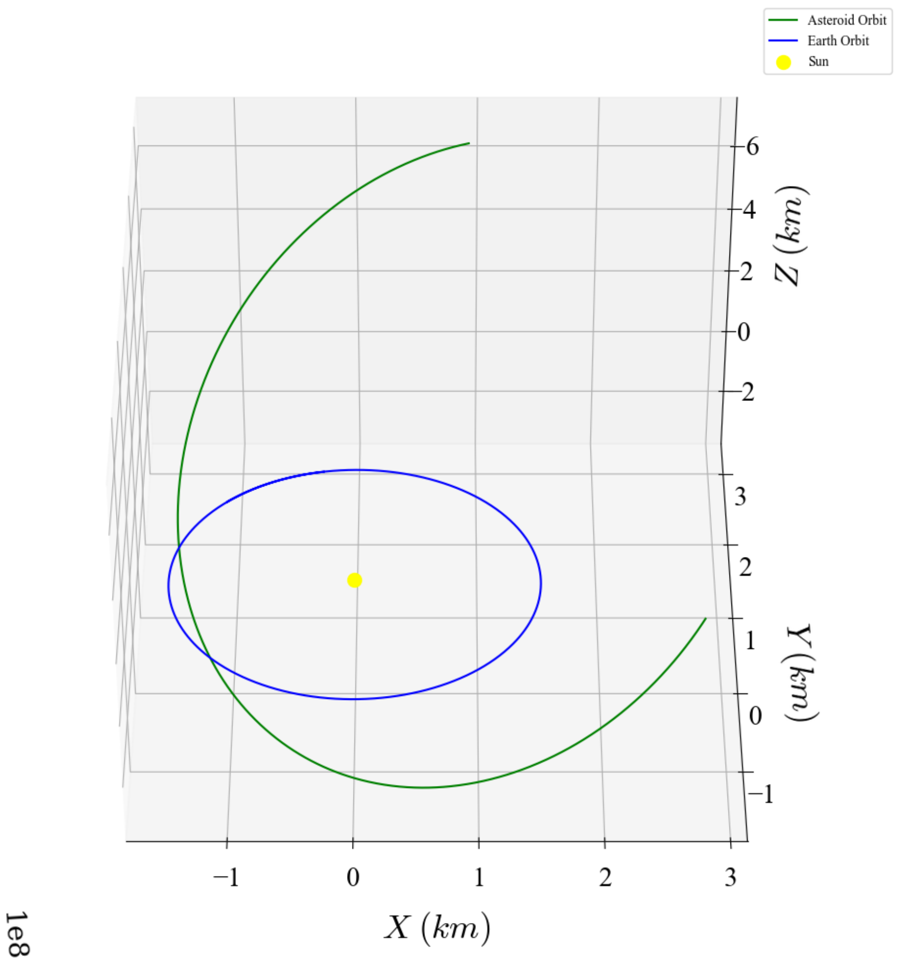

FIGURE 6.2: Trajectory of 1950DA relative to the Sun and Earth.

The results of this simulation show that no particles remain in a stable orbit around 1950DA when considering solar radiation pressure and 3^{rd} body perturbations from the Sun. When considering only solar radiation pressure, some larger radius particles do remain in orbit for the length of the simulation, however these escape the Hill sphere of the asteroid when the 3^{rd} body perturbations are taken into account. This shows that even though a ring-like structure may form around the asteroid, it is not stable and will eventually dissipate due to these perturbations. However, this yields several possibilities for the conclusion and leaves room for future work. The first possibility is that 1950DA is not a rubble pile asteroid and in fact a solid structure, as this fast rotation would cause any loose material to escape the surface and cause 1950DA to be non-existent otherwise. Another possibility is that the particles that escape the surface are do form a ring structure, however this ring is not stable over long periods of time. This can be examined in future work by including other perturbations such as the gravitational effects of other planets, or the Yarkovsky effect (Aljbaae et al., 2020). This would mean that the ring structure is only temporary and would eventually dissipate over time, with the particles colliding back to the surface of the asteroid or escaping the Hill sphere. However, given this current work it can be stated that the possibility of a stable ring structure around 1950DA is very unlikely or that 1950DA itself is not a rubble pile asteroid. There is also a possibilities that the surface is ever changing from our first glimpse at 1950DA with the partciles escaping.

Chapter 7

Final Remarks

7.1 MASCON Model Creation & Results Summary

The MASCON model is a balance between accuracy and efficient computational load compared to other methods like spherical harmonics and polyhedron models. The model can be created from OBJ shape files, with the accuracy depending on what we can perceive at a distance. This gives way to the crucial understanding that these programs for modeling and simulating orbits will be run iteratively on-board spacecraft on approach to these target asteroids. By implementing multiprocessing these software can be run in a reasonable time frame, allowing for real-time navigation and mission planning on-board spacecraft and independently from ground based calculations.

The work by Aljbaae et al. (2020) on Apophis served as a mathmatical check on the MASCON models created in this work. Results showed that the MASCON model is correct, and more detailed Poincaré sections were created to show the complex dynamics around Apophis. The use of multiprocessing and OSCER allowed for faster computation times, and allowed for these sections to be more detailed than previously shown in literature. The MASCON model of 1950DA was then created and utilized to study the small body dynamics around the asteroid. The results of this showed stable regions around the asteroid along with islands of stability with a possible $1:4$ resonant orbit. Refining the initial conditions in future work will allow this resonant orbit's position to be confirmed and used for mission planning. The presence of stability in high energy regions around 1950DA is promising for future mission designs as these can be utilized for missions that require short travel times at a high energy or velocity.

Examining the equilibrium points of 1950DA showed that the asteroid has internal equilibrium, serving as a check on the software, yet no external equilibrium points were found in either the 2-Dimensional planes or in 3-Dimensions. This is due to the fast rotation of the asteroid, which creates a complex gravitational field that is highly chaotic in several regions.

The Negri-Prado control law was then implemented to begin a mission design for 1950DA. The results show a capture from a high energy escape trajectory, with a minimum ΔV usage of only 0.85435 m/s. A scanning orbit was then designed to observe the surface of the asteroid, allowing for a more detailed model to be created from the scans. Then a landing trajectory was designed to bring the spacecraft to the surface of the asteroid, with a total ΔV usage of 1.455312 m/s considering a transfer from the high energy capture orbit. This showed the feasibility of a mission to 1950DA using low thrust propulsion, and future work can consider optimizing these trajectories further to reduce the ΔV usage. This would allow for more efficient mission planning and save cost on fuel which is a crucial aspect of any mission design.

Machine learning was utilized to reduce the number of MASCONs in the model of 1950DA and subsequently reduced computation time by 16.1 % for a 50 % reduction in MASCONs. The results showed that short term accuracy was very good, with the error remaining below 1 % for almost a day, however these results are not suitable for long term simulations as the error grows to 20 % after 3 $days$ of simulation time. With further work, this would allow on-board computations to be sped up further, allowing for optimal real-time navigation and supports the iterative nature of asteroid modeling on approach to the target.

Finally, the possibility of a ring structure around 1950DA was explored by simulating surface particles and observing their behavior over time. The results showed that some particles do escape the surface and form a ring-like structure, however when considering solar radiation pressure and 3^{rd} body perturbations from the Sun, no particles remain in a stable orbit around 1950DA. This shows that even though a ring-like structure may form around the asteroid, it is not stable and will eventually dissipate due to these perturbations. However, this yields several possibilities for the conclusion and leaves room for future work. The first possibility is that 1950DA is not a rubble pile asteroid and in fact a solid structure, as this fast rotation would cause any loose material to escape the surface and cause 1950DA to be non-existent otherwise. The other is that 1950DA has an ever changing shape due to its fast rotation and the loose material on the surface is constantly shifting and re-settling. This would cause particles to be ejected from the surface and leave the SOI making the mass and shape smaller, or even cause particles to re-impact the surface after being ejected creating new shapes with each new impact. Future work can consider modeling this behavior and observing the long-term dynamics of surface particles on 1950DA to better understand the nature of this asteroid.

Appendix A

Simulation Code

A.1 Accessing simulations and code

My thesis makes use of several custom codes and simulations developed over the course of my research. The software that is currently public includes:

- Negri-Prado Control Law: https://github.com/evan-a-blosser-1/Negri-Prado-Control-Law
- Asteroid MASCON model generator & Main simulation for personal PC or OCSER: https://github.com/evan-a-blosser-1/AMON
- Asteroid ring analysis simulation: https://github.com/evan-a-blosser-1/Ring-Analysis

Access to any of these resources not currently public can be provided upon request. Request can be made through the following emails:

- evan.a.blosser-1@ou.edu
- evan.blosser1@gmail.com

Please feel free to contact me directly via email, you can also visit my GitHub page at:

- https://github.com/evan-a-blosser-1

Or my GitHub website at:

- https://evan-a-blosser-1.github.io/

Bibliography

Aljbaae, S. et al. (Oct. 2016). "The dynamical environment of asteroid 21 Lutetia according to different internal models". In: *Monthly Notices of the Royal Astronomical Society* 464.3, pp. 3552–3560. ISSN: 1365-2966. DOI: 10.1093/mnras/stw2619.

Aljbaae, S. et al. (2020). *First approximation for spacecraft motion relative to (99942) Apophis*. DOI: 10.48550/ARXIV.2012.06781.

Antoni, Markus (Sept. 2022). "A review of different mascon approaches for regional gravity field modelling since 1968". In: *History of Geo- and Space Sciences* 13.2, pp. 205–217. ISSN: 2190-5029. DOI: 10.5194/hgss-13-205-2022.

Bate, Roger R. (2020). *Fundamentals of astrodynamics*. Ed. by Donald D. Mueller, Jerry E. White, and William W. Saylor. Second edition. "This Dover edition, first published in 2020, is a revised and updated second edition of the work originally published by Dover in 1971." - Impressum. Mineola, New York: Dover Publications, Inc. 417 pp. ISBN: 0486497046.

Batista Negri, Rodolfo and Antônio F. B. A. Prado (Mar. 2022). "Autonomous and Robust Orbit-Keeping for Small-Body Missions". In: *Journal of Guidance, Control, and Dynamics* 45.3, pp. 587–598. ISSN: 1533-3884. DOI: 10.2514/1.g005863.

Benner, Lance A.M. (n.d.). *Asteroid radar research*. URL: https://echo.jpl.nasa.gov/.

Benson, Conor J. et al. (Jan. 2023). "Spin state evolution of (99942) Apophis during its 2029 Earth encounter". In: *Icarus* 390, p. 115324. ISSN: 0019-1035. DOI: 10.1016/j.icarus.2022.115324.

Broer, Henk W., George B. Huitema, and Mikhail B. Sevryuk (2009). *Quasi-Periodic Motions in Families of Dynamical Systems: Order amidst Chaos*. Dordrecht: Springer.

BUSCH, M et al. (Oct. 2007). "Physical modeling of near-Earth Asteroid (29075) 1950 DA". In: *Icarus* 190.2, pp. 608–621. ISSN: 0019-1035. DOI: 10.1016/j.icarus.2007.03.032.

Curtis, Howard (2020). *Orbital Mechanics for Engineering Students Revised Reprint. Revised Reprint*. Elsevier Science Technology. ISBN: 9780128240250.

Farnocchia, D. and S.R. Chesley (Feb. 2014). "Assessment of the 2880 impact threat from Asteroid (29075) 1950 DA". In: *Icarus* 229, pp. 321–327. ISSN: 0019-1035. DOI: 10.1016/j.icarus.2013.09.022.

Frieger, Greg (accessed 2025). *3D Asteroid Catalogue*. https://3d-asteroids.space/. Interactive catalogue of 3D models, orbital and physical parameters of asteroids and other minor bodies.

Giorgini, J. D. et al. (Apr. 2002). "Asteroid 1950 DA's Encounter with Earth in 2880: Physical Limits of Collision Probability Prediction". In: *Science* 296.5565, pp. 132–136. ISSN: 1095-9203. DOI: 10.1126/science.1068191.

Haug, Espen Gaarder (Aug. 2022). "Progress in the Composite View of the Newton Gravitational Constant and Its Link to the Planck Scale". In: *Universe* 8.9, p. 454. ISSN: 2218-1997. DOI: 10.3390/universe8090454.

Jet Propulsion Laboratory, California Institute of Technology (2025). *NASA Aims to Fly First Quantum Sensor for Gravity Measurements*. https://www.jpl.nasa.gov/news/nasa-aims-to-fly-first-quantum-sensor-for-gravity-measurements/. JPL news release; accessed September 2025.

Jiang, Yu et al. (Sept. 2013). "Orbits and manifolds near the equilibrium points around a rotating asteroid". In: *Astrophysics and Space Science* 349.1, pp. 83–106. ISSN: 1572-946X. DOI: 10.1007/s10509-013-1618-8.

MacMillan, William Duncan (1958a). *The Theory of the Potential*. Dover Publications, Inc.

— (1958b). *The Theory of the Potential*. Dover Publications, Inc.

Mirtich, Brian (Jan. 1996). "Fast and Accurate Computation of Polyhedral Mass Properties". In: *Journal of Graphics Tools* 1.2, pp. 31–50. ISSN: 1086-7651. DOI: 10.1080/10867651.1996.10487458.

Moehlis, Jeff, Kresimir Josic, and Eric T. Shea-Brown (2006). "Periodic orbit". In: *Scholarpedia* 1.7. Definition: "A periodic orbit corresponds to ... one which repeats itself in time.", p. 1358.

Muller, P. M. and W. L. Sjogren (Aug. 1968). "Mascons: Lunar Mass Concentrations". In: *Science* 161.3842, pp. 680–684. ISSN: 1095-9203. DOI: 10.1126/science.161.3842.680.

Murray, C. D. and S. F. Dermott (1999). *Solar System Dynamics*. Cambridge University Press.

NASA Science (2024). *OSIRIS-APEX Mission (Origins, Spectral Interpretation, Resource Identification and Security – Apophis Explorer)*. https://science.nasa.gov/mission/osiris-apex/. Page last updated July 2, 2024; accessed September 2025.

Negri, Rodolfo Batista and Antônio Fernando Bertachini de Almeida Prado (2020). *Robust Path-following for Keplerian Orbits*. DOI: 10.48550/ARXIV.2012.01954.

Newton, Isaac (1687). *Philosophiae naturalis principia mathematica*. Jussu Societatis Regiae ac Typis Josephi Streater. Prostat apud plures bibliopolas. DOI: 10.5479/sil.52126.39088015628399.

Newton, Isaac (1729). "The Mathematical Principles of Natural Philosophy". In: trans. by Andrew Motte. English translation of Newton's General Scholium, appended to Book III. London: Benjamin Motte.

Nolan, Michael C. et al. (Sept. 2013). "Shape model and surface properties of the OSIRIS-REx target Asteroid (101955) Bennu from radar and lightcurve observations". In: *Icarus* 226.1, pp. 629–640. ISSN: 0019-1035. DOI: 10.1016/j.icarus.2013.05.028.

Pravec, Petr and Alan W. Harris (Nov. 2000). "Fast and Slow Rotation of Asteroids". In: *Icarus* 148.1, pp. 12–20. ISSN: 0019-1035. DOI: 10.1006/icar.2000.6482.

Raschka, Sebastian (2022). *Machine Learning with PyTorch and Scikit-Learn. Develop machine learning and deep learning models with Python*. Ed. by Yuxi Liu, Vahid Mirjalili, and Dmytro Dzhulgakov. 1. Birmingham: Packt Publishing Limited. 1770 pp. ISBN: 9781801816380.

Rozitis, Ben, Eric MacLennan, and Joshua P. Emery (Aug. 2014). "Cohesive forces prevent the rotational breakup of rubble-pile asteroid (29075) 1950 DA". In: *Nature* 512.7513, pp. 174–176. ISSN: 1476-4687. DOI: 10.1038/nature13632.

Scheeres, Daniel J. (2012). *Orbital Motion in Strongly Perturbed Environments. Applications to Asteroid, Comet and Planetary Satellite Orbiters*. SpringerLink. Berlin, Heidelberg: Springer Berlin Heidelberg. 390 pp. ISBN: 9783642032561.

The Planetary Society (2025). *Asteroid Apophis: Will It Hit Earth? Your Questions Answered*. https://www.planetary.org/articles/will-apophis-hit-earth. Web article accessed September 2025.

Tsoulis, Dimitrios and Georgia Gavriilidou (Sept. 2021). "A computational review of the line integral analytical formulation of the polyhedral gravity signal". In: *Geophysical Prospecting* 69.8–9, pp. 1745–1760. ISSN: 1365-2478. DOI: 10.1111/1365-2478.13134.

Tsoulis, Dimitrios and Sveto Petrović (Mar. 2001). "On the singularities of the gravity field of a homogeneous polyhedral body". In: *GEOPHYSICS* 66.2, pp. 535–539. ISSN: 1942-2156. DOI: 10.1190/1.1444944.

U.S. Naval Observatory (2021). *Constants 2021*. https://aa.usno.navy.mil/downloads/publications/Constants_2021.pdf. Accessed: insert access date.

Vallado, David A. (2022). *Fundamentals of astrodynamics and applications*. Fifth edition, first printing. Space technology library 21. Torrance, CA: Microcosm Press. 1122 pp. ISBN: 9781881883197.

Winter, Othon C. and Carl D. Murray (1994). *Atlas of the Planar, Circular Restricted Three-Body Problem. Othon C.* Vol. 1. QMW maths notes 16. London: School of Mathematical Sciences, Queen Mary and Westfield College. 397 pp. ISBN: 0902480154.

Ďurech, J., V. Sidorin, and M. Kaasalainen (Apr. 2010). "DAMIT: a database of asteroid models". In: *Astronomy and Astrophysics* 513, A46. ISSN: 1432-0746. DOI: 10.1051/0004-6361/200912693.